

# DISSOCIATIONS BETWEEN MICROSTRUCTURAL AND FUNCTIONAL HIERARCHIES WITHIN REGIONS OF TRANSMODAL CORTEX

PAQUOLA C<sup>1</sup>, VOS DE WAELE R<sup>1</sup>, WAGSTYL K<sup>2</sup>, BETHLEHEM RAI<sup>3</sup>, HONG SJ<sup>1</sup>, SEIDLITZ J<sup>4,5</sup>, BULLMORE ET<sup>5</sup>, EVANS AC<sup>1,2</sup>, MISIC B<sup>1</sup>, MARGULIES DS<sup>6</sup>, SMALLWOOD J<sup>7</sup>, BERNHARDT BC<sup>1\*</sup>

<sup>1</sup> McConnell Brain Imaging Centre, Montreal Neurological Institute and Hospital, McGill University, Montreal, QC, Canada; <sup>2</sup> McGill Centre for Integrative Neuroscience, McGill University, Montreal, QC, Canada; <sup>3</sup> Autism Research Centre, Department of Psychiatry, University of Cambridge, England, United Kingdom; <sup>4</sup> Developmental Neurogenetics Unit, National Institute of Mental Health, Bethesda, MD 20892, USA; <sup>5</sup> Brain Mapping Unit, University of Cambridge, Department of Psychiatry, Cambridge CB2 0SZ, UK; <sup>6</sup> Frontlab, Institut du Cerveau et de la Moelle épinière, UPMC UMRS 1127, Inserm U 1127, CNRS UMR 7225, Paris, France; <sup>7</sup> York Neuroimaging Center, University of York, UK

## SUMMARY

While the role of cortical microstructure in organising neural function is well established, it remains unclear how structural constraints can give rise to more flexible elements of cognition. While non-human primate research has demonstrated a close structure-function correspondence, the relationship between microstructure and function remains poorly understood in humans, in part because of the reliance on *post mortem* analyses which cannot be directly related to functional data. To overcome this barrier, we developed a novel approach to model the similarity of microstructural profiles sampled in the direction of cortical columns. Our approach was initially formulated based on an ultra-high-resolution 3D histological reconstruction of an entire human brain and then translated to myelin-sensitive MRI data in a large cohort of healthy adults. This novel method identified a system-level gradient of microstructural differentiation traversing from primary sensory to limbic regions that followed shifts in laminar differentiation and cytoarchitectural complexity. Importantly, while microstructural and functional gradients described a similar hierarchy, they became increasingly dissociated in transmodal default mode and fronto-parietal networks. Meta analytic decoding of these topographic dissociations highlighted associations with higher-level aspects of cognition such as cognitive control and social cognition. Our findings demonstrate a relative decoupling of macroscale function from cortical microstructure in transmodal regions, which likely contributes to the flexible role these regions play in human cognition.

## KEY WORDS

Microstructure, histology, MRI, neuroimaging, structure-function, connectome, hierarchy

## CORRESPONDING AUTHORS

Boris Bernhardt [boris.bernhardt@mcgill.ca](mailto:boris.bernhardt@mcgill.ca) (Lead Contact)  
Casey Paquola [casey.paquola@mail.mcgill.ca](mailto:casey.paquola@mail.mcgill.ca)

McConnell Brain Imaging Center  
Montreal Neurological Institute  
3801 University Street  
Montreal, QC, H3A2B4  
Canada

Tel. 514-398-3579

## INTRODUCTION

A core principle of neuroscience is that brain structure governs ongoing function. For decades, non-human primate work has confirmed the intrinsic relationship between microstructure and macrolevel function (1–3). While the role of structure in cortical processing is well characterised in the sensory-motor domain, it is less clear how this constraint gives rise to more flexible elements of cognition. In an attempt to describe how cortical areas are able to take on more abstract functional roles, Mesulam (1998) postulated a hierarchical axis of large-scale cortical organisation and connectivity, referred to as the “sensory-fugal gradient”. This axis describes gradual transitions at the whole-cortex level, running from primary sensory and motor regions that are involved in externally focussed computations towards transmodal cortices that are increasingly engaged in more perceptually decoupled operations. Unlike sensory cortices, transmodal cortices have a less hierarchical organisation (3,5–7) with a more parallel architecture that allows spatially distributed areas to respond flexibly to different types of information (8).

The current study systematically examined the interplay between microstructural constraints and functional connectivity in humans, and its contribution to high-level cognition and behaviour. Studying cortical microstructure in humans, neuroanatomists have traditionally used cell staining techniques to map spatial variations in both cyto- and myeloarchitectural features of *post mortem* brains (9–13). Extending upon this work, the ‘structural model’ proposes a principled relationship between microstructural similarity and large-scale connectivity of cortical areas (14), which was however primarily formulated based on non-human primate data. Notably, it holds greater predictive power in sensorimotor and unimodal association areas, compared to transmodal areas performing integrative cognitive operations. Although *post mortem* methods are the gold standard for describing microstructure per se, they cannot be mapped directly to function *in vivo*, making it hard to directly quantify how these metrics relate to neural function. With the advent of high-field magnetic resonance imaging (MRI), it has become possible to probe microstructural properties of different cortical regions in the living human brain. In particular, myelin sensitive imaging contrasts can differentiate regions with distinct myeloarchitectural profiles at an individual level (15–19). In parallel, resting-state functional MRI analysis can identify highly reproducible intrinsic networks formed by cortical areas (20–25). These studies have highlighted that transmodal cortex is largely composed of two spatially distributed yet functionally cohesive networks– the fronto-parietal network thought to respond to the demands of the moment in a flexible way (26–28) and the default mode network that depends on abstract information from self-generated memory and thought processes (29–31).

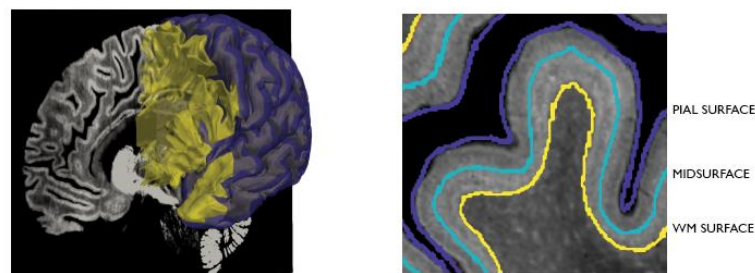
Core to our analysis was the formulation of a novel approach that modelled cortico-cortical networks from similarity of microstructural profiles sampled across thousands of points and in the direction of cortical columns. The model was first developed on an ultra-high resolution *post mortem* 3D histological reconstruction of an entire human brain (32), and we show robust evidence for a principal spatial axis of gradual cytoarchitectural variation running from primary sensory to transmodal areas, recapitulating established spatial trends in laminar differentiation and cytoarchitectural complexity (4,33). We then translated our approach to myelin-sensitive MRI in a large cohort of healthy adults, showing consistency *in vivo* and across individuals (34). In addition to showing correspondence between histological and MRI-derived topographies, microstructural gradients only partially converged with macroscale functional topographies derived from task-free functional connectome analysis obtained in the same subjects (25). In fact, while primary sensory regions served as a common anchor of microstructural and functional gradients, the microstructural axis depicted a progression towards limbic cortices, while its functional counterpart traversed towards default mode and fronto-parietal networks. Critically, meta-analytic decoding revealed that dissociation of function from microstructure was related to patterns of higher-order thought, such as a cognitive control or social cognition. Together our analyses on the convergence and divergence of spatial trends in microstructure and function support the hypothesis that reductions in the constraining influence of microstructure in transmodal cortex is a central underlying mechanism through which flexible cognitive functions may emerge.

## RESULTS

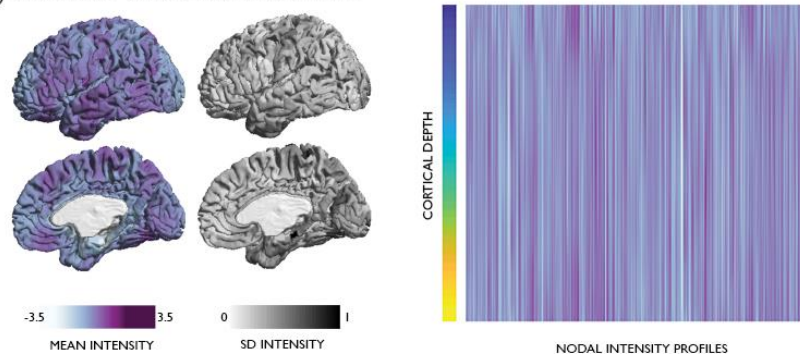
### Formulation of the histology-based microstructure profile covariance analysis

We modelled cortico-cortical microstructural similarity across a 100 $\mu$ m resolution Merker-stained 3D histological reconstruction of an entire *post mortem* human brain [BigBrain; <https://bigbrain.loris.ca/main.php>; (32) (FIGURE 1A)]. Staining intensity profiles, representing neuronal density and soma size by cortical depth, were generated along 160k surface points (*henceforth*, vertices) for each hemisphere (FIGURE 1B). Profile residuals, obtained after correcting intensity profile data for the y-coordinate to account for measurable shifts in intensity in anterior-to-posterior direction (SI FIGURE S1), were averaged within 1012 equally sized, spatially contiguous nodes (35). Pairwise correlations of nodal intensity profiles, covaried for average intensity profile, were thresholded at 0 and positive edges were log-transformed to produce a microstructure profile covariance matrix (MPC<sub>HIST</sub>); in other words, MPC<sub>HIST</sub> captures cytoarchitectural similarity between cortical areas (see SI FIGURE S2 for distribution of values).

#### A) CONSTRUCTION OF INTRACORTICAL SURFACES



#### B) MICROSTRUCTURE PROFILES



#### C) MICROSTRUCTURE PROFILE COVARIANCE (MPC<sub>HIST</sub>)

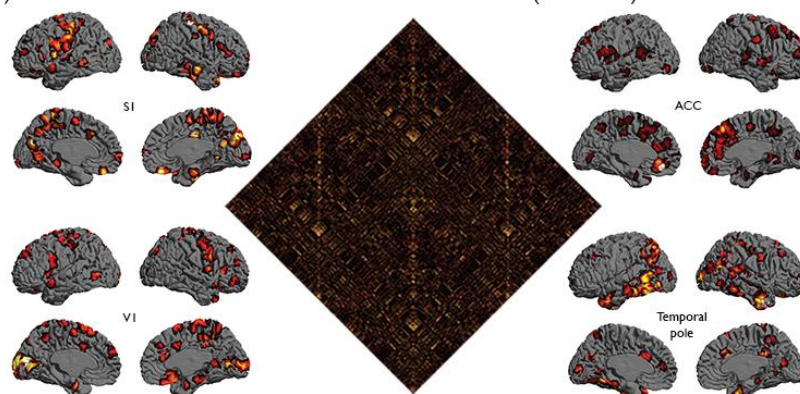


**FIGURE 1.** Histology-based microstructure profile covariance (MPC<sub>HIST</sub>) analysis. (A) Pial (purple) and white matter (WM: yellow) surfaces displayed against a sagittal slice of the BigBrain (left) and with the midsurface (blue) in magnified view (right). (B) Mean and standard deviation (SD) in residual intensity at each node are displayed on the cortex (left). Cortex-wide intensity profiles were calculated by systematic intensity sampling across intracortical surfaces (rows) and nodes (columns). (C) The MPC<sub>HIST</sub> matrix depicts node-wise partial correlations in intensity profiles, controlling for the average intensity profile. Exemplary patterns of microstructural similarity from primary somatosensory (S1), anterior cingulate cortex (ACC), primary visual (V1) and the temporal pole. Seed nodes are shown in white.



The pipeline was optimised with respect to the number of intracortical surfaces based on matrix stability (see **METHODS** and **SI FIGURE S3**). While microstructural similarity had a small but significant statistical relationship with spatial proximity (adjusted  $R^2=0.02$ ,  $p<0.001$ ), similar findings were obtained after correcting for geodesic distance.

**The principal gradient of microstructural similarity reflects sensory-fugal neurostructural variation**

Diffusion map embedding, a nonlinear dimensionality reduction algorithm (36) recently applied to identify an intrinsic functional segregation of cortical regions based on resting state functional MRI (25), was applied to the histology-based microstructure profile covariance matrix (**FIGURE 2A**). The relative positioning of nodes in this embedding space informs on (dis)similarity of their covariance patterns. The first principal gradient ( $G1_{HIST}$ ), accounting for 14.5% of variance, was anchored on one end by primary sensory and motor areas and on the other end by transmodal association and limbic cortices (**FIGURE 2B**; see **SI FIGURE S4** for the second gradient).  $G1_{HIST}$  depicted the most distinguishable transition in the shape of microstructure profiles (**FIGURE 2B RIGHT**). Regions of the prefrontal cortex (*green*) expressed an intracortical profile that was closest to the cortex-wide average. Extending outwards from centre of  $G1_{HIST}$ , sensory and motor regions (*blue-purple*) exhibited heightened cellular density around the midsurface, whereas paralimbic cortex (*red*) displayed specifically enhanced density near the cortical borders. For further validation of the biological basis of  $G1_{HIST}$ , we mapped independent atlases of laminar differentiation (37) and cytoarchitectural class (11,38) onto the BigBrain midsurface (**FIGURE 2C**).

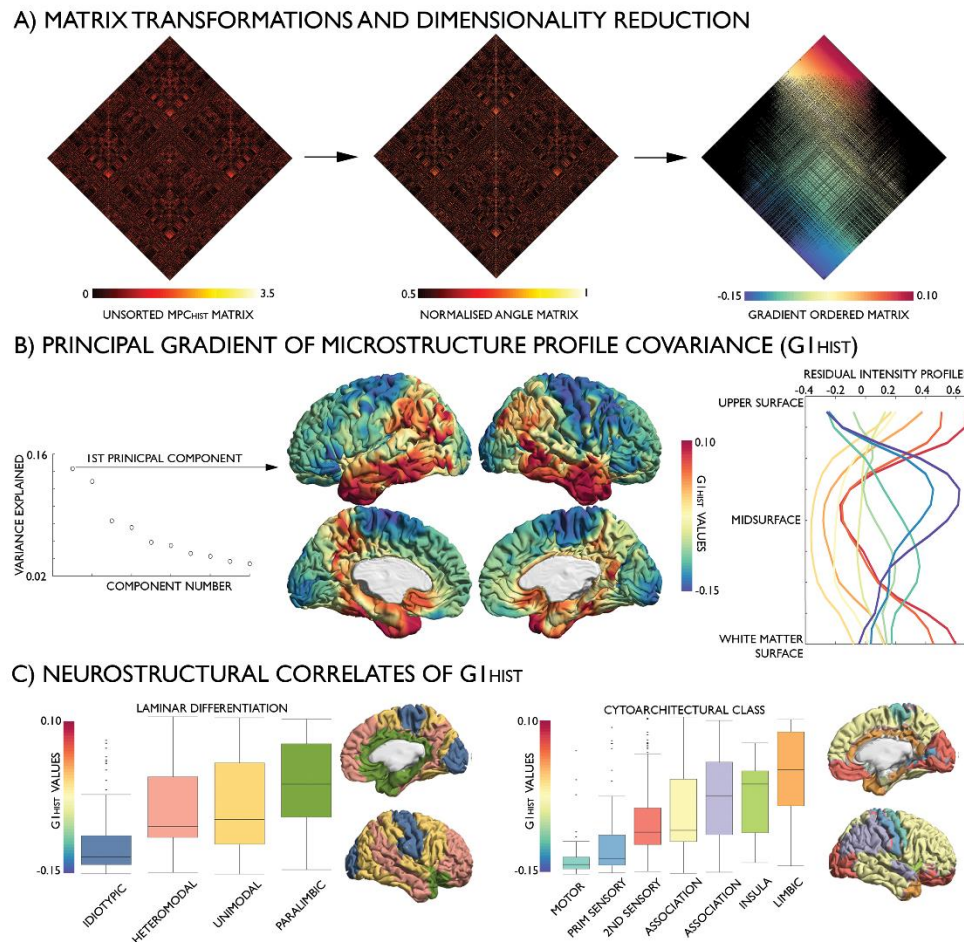


**FIGURE 2.** The principal gradient ( $G1_{HIST}$ ) of the histology-based microstructure profile covariance matrix ( $MPC_{HIST}$ ). **(A)** Identification: the  $MPC_{HIST}$  matrix was transformed into an affinity matrix, which captures similarities in microstructural profile covariance between nodes; this affinity matrix was subjected to diffusion map embedding, a non-linear compression algorithm that sorts nodes based on  $MPC_{HIST}$  similarity. **(B)** Variance explained by embedding components (*left*). The first component,  $G1_{HIST}$ , describes a gradual transition from primary sensory and motor (*blue*) to transmodal and limbic areas (*red*), corresponding to changes in intensity profiles, illustrated with the mean residual intensity profile across ten discrete bins of the gradient (*right*). **(C)** Spatial associations between  $G1_{HIST}$  and levels of laminar differentiation [*left*; (37)] and cytoarchitectural taxonomy [*right*; (11,38)], ordered by median.

Multiple regression analyses showed that levels of laminar differentiation and cytoarchitectural taxonomy each accounted for 17% of variance in  $G1_{HIST}$  (**SI TABLES S1-2**). Strongest predictors were idiosyncratic ( $\beta=0.06$ ,  $p<0.001$ ) and paralimbic ( $\beta=0.05$ ,  $p<0.001$ ) laminar differentiation levels, and limbic ( $\beta=0.07$ ,  $p<0.001$ ) as well as motor ( $\beta=0.06$ ,  $p<0.001$ ) classes in the cytoarchitectural model, demonstrating the cytoarchitectural distinctiveness of regions at the extremes of  $G1_{HIST}$ .

#### Development of in vivo microstructure profile covariance analysis

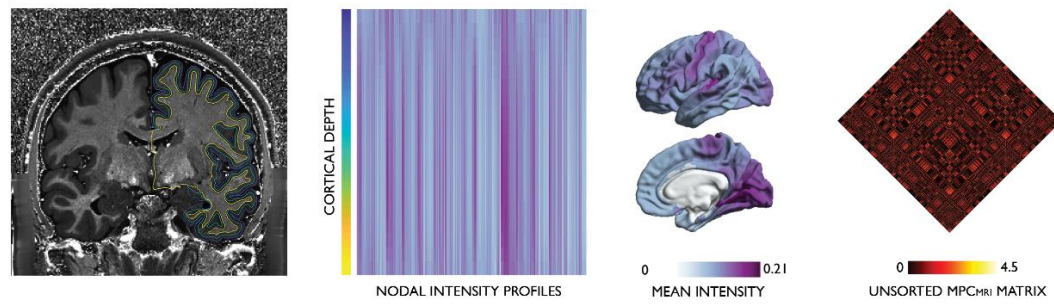
The microstructure profile covariance approach was adapted to *in vivo* data in single individuals using T1w/T2w MRI, a ratio indexing cortical microstructure and myelin (15), shown to recapitulate sensory-fugal transitions (39). Multimodal surface-matched T1w/T2w images, pial surfaces, and white matter surfaces were obtained from the minimally-preprocessed S900 release of the Human Connectome Project (34,40). We selected a total of 219 unrelated subjects and grouped these randomly into a *Discovery* sample ( $n=110$ , 66 females, mean $\pm$ SD age=28.8 $\pm$ 3.8 years) and a *Replication* sample ( $n=109$ , 62 females, mean $\pm$ SD age=28.5 $\pm$ 3.7 years). For each individual, we systematically generated intracortical surfaces using the same equivolumetric transformation algorithm as for the histological dataset (41,42), and aggregated whole cortex intensity profiles across 64,984 linked vertices that were subsequently parcellated into 1012 contiguous nodes (35). We computed pairwise partial correlations between nodal intensity profiles (controlling for the average intensity profile), kept only positive correlations, and log-transformed the result to produce a cortex-wide microstructure profile covariance matrix ( $MPC_{MRI}$ ; see **SI FIGURE S5** for distribution of values). A group-average  $MPC_{MRI}$  matrix was calculated across all participants in the *Discovery* sample. While microstructural similarity estimated *in vivo* was stronger between proximal nodes, the variance accounted for by geodesic distance was low (adjusted  $R^2 = 0.04$ ,  $\beta=-2.57$ ,  $p<0.001$ ).

Diffusion map embedding revealed a principal gradient of microstructural differentiation accounting for 13.7% of variance ( $G1_{MRI}$ , **FIGURE 3B**; see **SI FIGURE S6** for the second gradient). In line with its histological counterpart,  $G1_{MRI}$  was anchored on one end by primary sensory areas and on the other end by limbic regions. Cortex-wide analysis demonstrated a high correlation of  $G1_{HIST}$  and  $G1_{MRI}$  ( $r=0.63$ ,  $p<0.001$ ), driven by the close spatial correspondence of gradient extremes (**FIGURE 3C, left**).  $G1_{MRI}$  depicts increasing mean myelin content, as well as a gradual transition in the relative myelin content around the midsurface (**FIGURE 3B, right**). Microstructural profiles of the prefrontal cortex (*orange*) again resembled the cortex-wide average; however, comparing node ranks across both modalities revealed a shift in prefrontal regions towards the transmodal anchor in  $G1_{MRI}$  (**FIGURE 3C, right**). This effect appeared to be driven by a downward shift of lateral occipital-parietal areas towards the sensory anchor, owing to heavy myelination relative to their cytoarchitectural complexity (43). Laminar differentiation and cytoarchitectural taxonomy accounted for 44% and 37% of variance in  $G1_{MRI}$ , respectively (**SI TABLES S3-4**). As in the histological analysis, the paralimbic ( $\beta=0.10$ ,  $p<0.001$ ) and idiosyncratic ( $\beta=0.07$ ,  $p<0.001$ ) levels were the strongest predictors within the laminar differentiation model, while motor ( $\beta=0.15$ ,  $p<0.001$ ), limbic ( $\beta=0.07$ ,  $p<0.001$ ), and primary sensory ( $\beta=0.10$ ,  $p<0.001$ ) classes were strong predictors within the cytoarchitectural model.

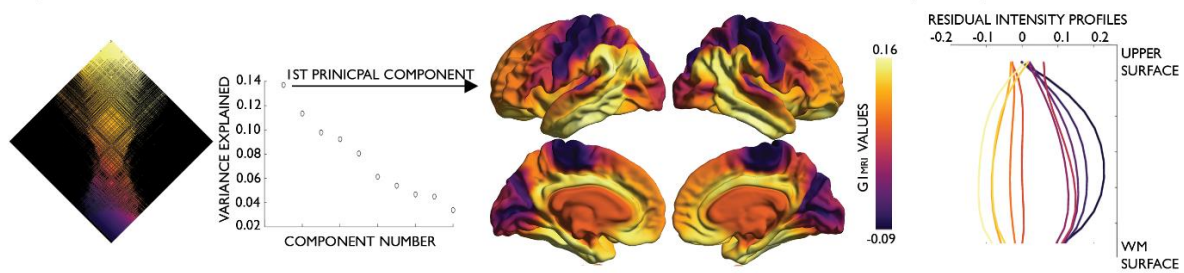
#### Correspondence of microstructural similarity with macroscale functional organisation

To examine the role of microstructural similarity in macroscale functional organisation, we generated a group-average resting state functional connectome across the *Discovery* subsample and derived gradients with diffusion map embedding. As shown previously (25), the principal functional gradient ( $G1_{FUNC}$ ) extends from primary sensory and motor networks, through dorsal attention and salience networks, to finally culminate in the transmodal core composed of fronto-parietal and default mode networks (**FIGURE 4A**). At the group level, cortex-wide analyses demonstrated moderate-to-high correlations of  $G1_{MRI}$  with  $G1_{FUNC}$  ( $r=0.52$ ,  $p<0.001$ ; **FIGURE 4B**) and  $G1_{HIST}$  with  $G1_{FUNC}$  ( $r=0.31$ ,  $p<0.001$ ), illustrating a common topography of microstructural profile covariance and functional connectivity. Notably, the topographies of microstructure and function were more closely related than node-to-node correspondence of microstructural similarity with functional connectivity (*in vivo*:  $r=0.10$ ,  $p<0.001$ ; histology-based:  $r=0.11$ ,  $p<0.001$ ), supporting the utility of connectivity-informed dimensionality reduction techniques to reveal common principles of sensory-fugal cortical organisation (44).

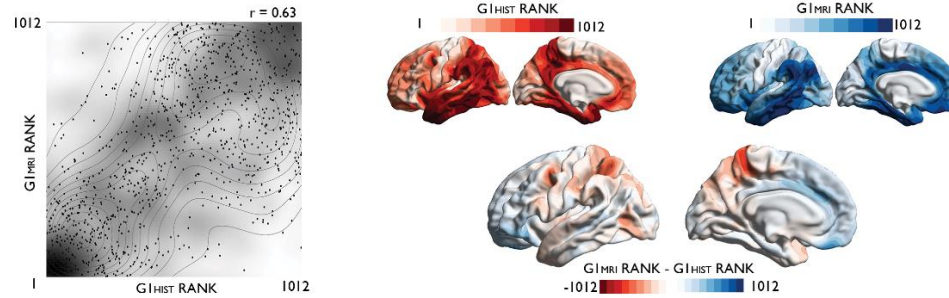
### A) IN-VIVO SURFACE CONSTRUCTION AND SAMPLING



### B) IN VIVO GRADIENT OF MICROSTRUCTURE PROFILE COVARIANCE (G<sub>I</sub>MRI)



### C) RELATION OF G<sub>I</sub>MRI TO G<sub>I</sub>HIST



### D) NEUROSTRUCTURAL CORRELATES OF G<sub>I</sub>MRI

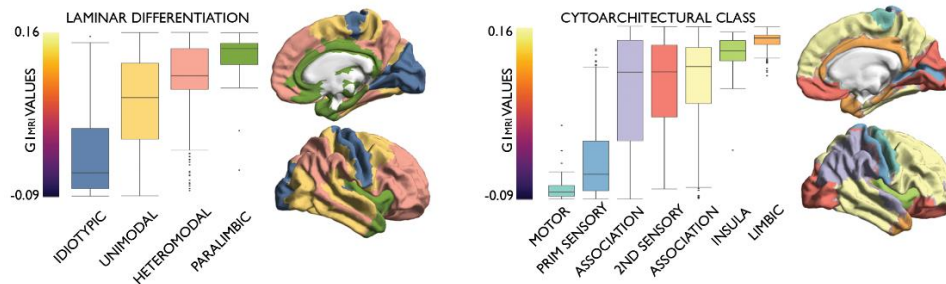
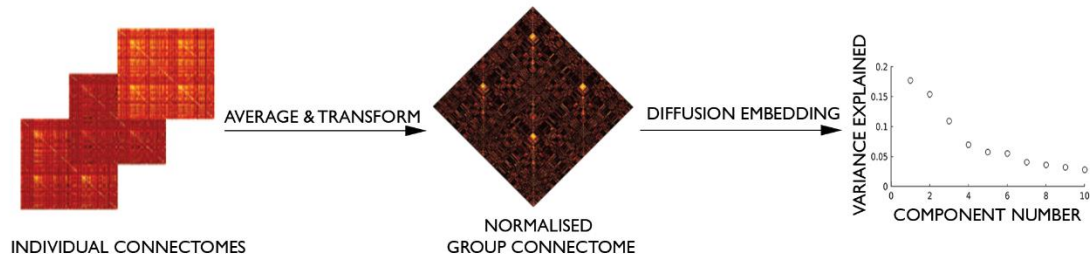


**FIGURE 3.** *In vivo* microstructure profile covariance (MPC<sub>MRI</sub>). (A) Left hemisphere pial, mid, and white matter surfaces superimposed on T1w/T2w image (left); whole-cortex intensity profiles were calculated by systematic sampling across surfaces (rows) and vertices, and then averaged with each node (columns). Mean at each node (centre right); MPC<sub>MRI</sub> matrix depicts node-wise partial correlations in intensity profiles, covaried for mean whole-cortex intensity profile (right). (B) Normalised angle matrix sorted by the principal gradient (left); variance explained by the diffusion embedding components (left centre) and the principal gradient (right centre); mean residual intensity profiles within ten discrete bins of the gradient (right). (C) Similarity of histological and *in vivo* gradients (G<sub>I</sub>HIST, G<sub>I</sub>MRI) shown in a density plot (left) and node-wise rank differences shown on the cortical surfaces (right). (D) Associations of G<sub>I</sub>MRI to levels of laminar differentiation (37) and cytoarchitectural class (11,38) ordered by median.

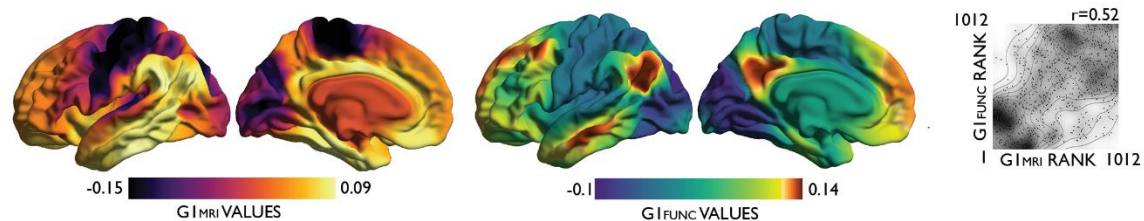


The *Replication* dataset underwent identical processing procedures as the *Discovery* dataset. At a group level,  $G1_{MRI}$  derived from the *Replication* and *Discovery* cohorts were highly correlated ( $r=0.98$ ,  $p<0.001$ ). High correlations between  $G1_{MRI}$  and  $G1_{FUNC}$  were also evident at the individual subject level, following alignment of individual functional and microstructural gradients to templates built from the group *Discovery* dataset (see **METHODS**, for details). For every participant, we observed a significant correlation between  $G1_{MRI}$  and  $G1_{FUNC}$  ( $0.37<r<0.61$ ,  $p<0.001$ ; **FIGURE 4C-D**).

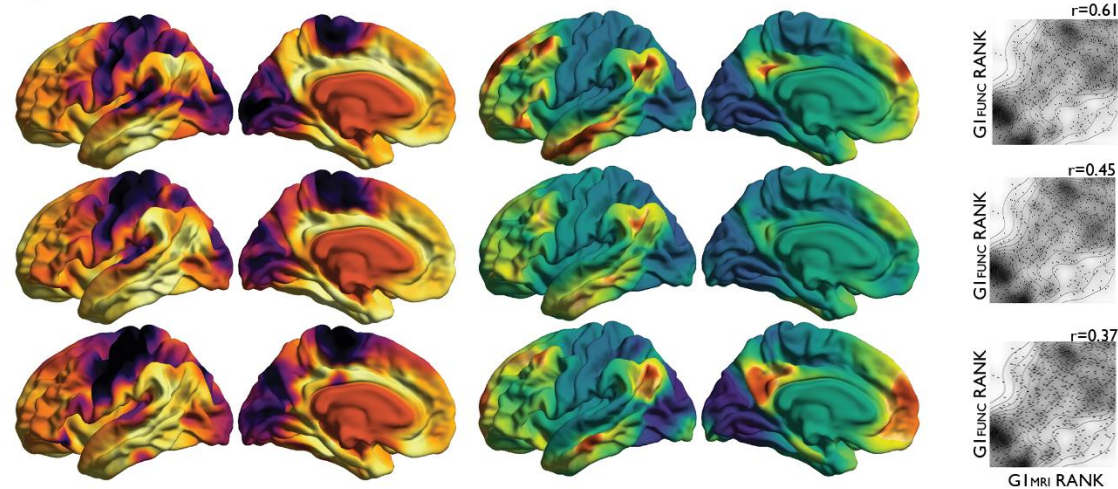
### A) CONSTRUCTION OF FUNCTIONAL GRADIENT ( $G1_{FUNC}$ )



### B) GMRI-GFUNC CORRESPONDENCE: GROUP LEVEL



### C) INDIVIDUALISED $G1_{MRI}$ AND $G1_{FUNC}$



### D) INTER-INDIVIDUAL VARIABILITY IN $G1_{MRI}$ AND $G1_{FUNC}$

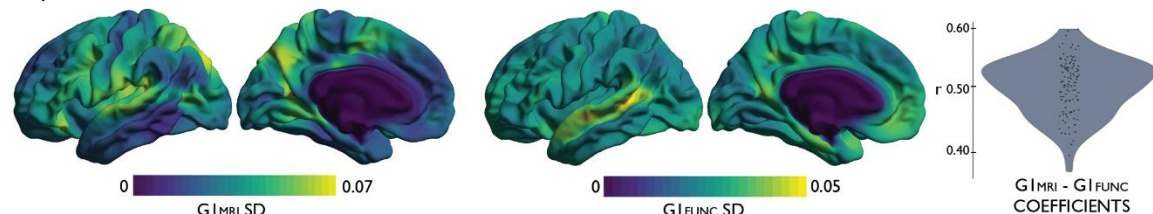


**FIGURE 4.** Cross-modal correspondence of the  $MPC_{MRI}$  and intrinsic functional gradients. (A) Transformation from individual functional connectomes (*left*) to a group average normalised angle matrix (*centre*) to diffusion embedding components (*right*) (B) The group level  $G1_{MRI}$  (*left*), group level  $G1_{FUNC}$  (*centre*) and density plots depicting the correlation between the gradients (*right*). (C) Consistency across 3 example subjects and (D) inter-individual variability of the gradients and cross-modal correspondence in the *Replication* dataset.

In addition to studying their commonalities, we assessed unique topographic features of the modality-specific gradients. Cortex-wide nodal rank comparisons highlighted an upward shift in the position of the prefrontal cortex and precuneus in functional gradient space, relative to the microstructure-derived gradient, and a converse downward shift of the posterior inferior temporal and midcingulate cortices (**FIGURE 5A**). Notably, the greatest rank differences were evident in transmodal cortices, suggesting a specific dissociation of function from microstructure in these higher-order regions. Inspecting the distribution of nodes in intrinsic functional communities (23) along each gradient (**FIGURE 5B**), we noted that while the sensory-fugal gradient was overall preserved across all modalities, different sensory and transmodal networks occupied extremes in each modality.  $G1_{MRI}$  extended from somatomotor to limbic networks, whereas  $G1_{FUNC}$  extended from visual to transmodal default mode networks. Comparing the average node rank of each functional community, between modalities and across individuals (**SI TABLE S5**), we noted that the default mode and fronto-parietal networks shifted to the apex of  $G1_{FUNC}$ , reflecting segregation of higher-order communities during rest, despite their similar myeloarchitecture.

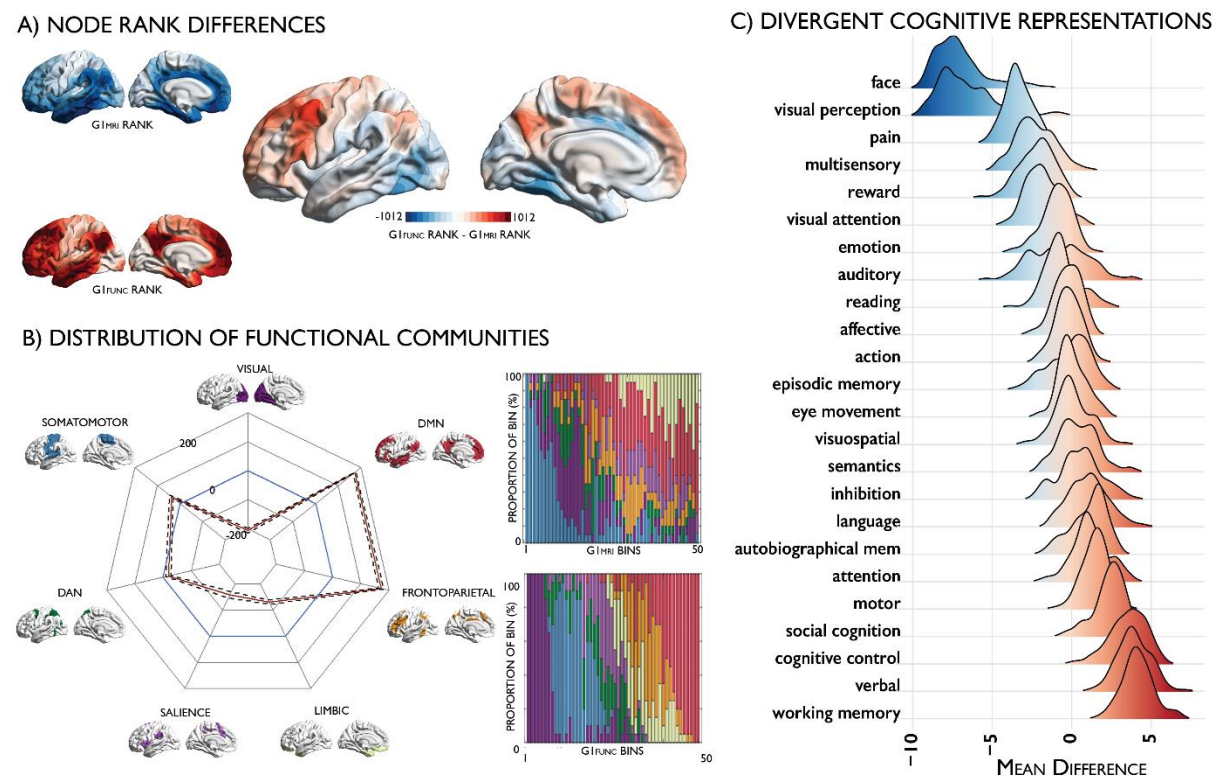


**FIGURE 5.** Divergent representations of the cortical hierarchy derived from microstructure and function. **(A)** Differences in nodal ranks between  $G1_{MRI}$  (blue) and  $G1_{FUNC}$  (red). **(B)** Stacked bar plots depicting the proportion of each bin accounted for by intrinsic functional communities (23); radar plot depicting the difference in mean node ranks of functional communities between  $G1_{MRI}$  (blue) and  $G1_{FUNC}$  (red), with 95% confidence intervals calculated across individuals presented with dotted lines. **(C)** Mean difference in the centre of gravity of meta-analysis maps in  $G1_{FUNC}$  and  $G1_{MRI}$  space, mapped as density plots illustrating the range of differences across subjects.

Our final analysis examined whether the functional topography diverged from microstructure specifically in cortical areas involved in abstract, perceptually decoupled functions. We conducted a meta-analysis using the Neurosynth database and estimated the centre of gravity across a set of diverse cognitive terms (25) along  $G1_{FUNC}$  relative to  $G1_{MRI}$  (**SI FIGURE 5C**). As hypothesised, the top terms exhibiting the strongest upward shift from  $G1_{MRI}$  to  $G1_{FUNC}$  involved multi-domain, integrative functions, such as “working memory”, “verbal”, “cognitive control” and “social control”, whereas the strongest downward shifts involved second-order visual processing, such as “face” and “visual perception”.



### Robustness of the MPC and resultant gradients

A series of replication analyses assessed the robustness of the MPC framework.

*a) Histology.*  $G1_{\text{HIST}}$  was highly consistent across variations in thresholding, parcellation, intracortical surface number, and BigBrain voxel resolution (**SI FIGURE S3**). Furthermore, varying the  $\alpha$  parameter for diffusion map embedding algorithm from 0 and 1 (in increments of 0.1) resulted in virtually identical gradients (all  $r > 0.99$ ). We also compared diffusion map derived gradients to more conventional graph theoretical characterisations of the  $\text{MPC}_{\text{HIST}}$  matrix. Specifically, we applied Louvain modularity detection (45), incorporating a procedure that maximized consensus across fine- and coarse-grained decompositions (by varying the tuning parameter  $\gamma$  from 0.5-1.5) across 100 repetitions. We resolved three modules ( $0.49 < Q < 0.71$ ; **SI FIGURE S7**), which occupied distinct positions along the first two gradients. Diffusion map embedding thus represents a continuous and complementary approach to order microstructure profile covariance, which emphasises gradual transitions within and between discrete cortical areas that are fundamental to the hierarchical organisation of layer-specific cortical projections (46).

*b) In vivo.* As for their histological counterpart,  $G1_{\text{MRI}}$  solutions were robust against processing parameter variation, including matrix thresholding, parcellation scheme, and surface number (**SI FIGURE S8**). Again, variation of the  $\alpha$  parameter resulted in virtually identical gradients (all  $r > 0.99$ ). Application of Louvain community detection identified only two modules in the microstructure profile covariance matrix which concisely halved  $G1_{\text{MRI}}$  ( $0.35 < Q < 0.41$ , **SI FIGURE S9**). We replicated  $G1_{\text{MRI}}$  in an independent dataset of healthy late adolescents/young adults (47) that underwent magnetisation transfer imaging (spatial correlation:  $r = 0.78$ ,  $p < 0.001$ , **SI FIGURE S10**) and in a cohort of 17 healthy adults scanned at our imaging centre in whom quantitative T1 relaxation data was available (spatial correlation:  $r = 0.81$ ,  $p < 0.001$ , **SI FIGURE S11**), demonstrating robustness of the approach to acquisition site, acquisition type, and surface construction.

## DISCUSSION

Cortical areas identified by classical neuroanatomical studies represent discrete regions embedded within gradual transitions in cyto- and myeloarchitecture (9–11,48). Cortical gradients are nearly ubiquitous across microstructural and functional domains of the mammalian neocortex, where mounting evidence supports a common and overarching “sensory-fugal” organisation (46,49). Leveraging a ultra-high-resolution 3D reconstruction of an entire *post mortem* human brain (32), we sampled microstructure profiles and utilised unsupervised techniques to identify smooth transitions in cytoarchitectural composition. We translated our approach from histology to myelin-sensitive *in vivo* MRI and recovered similar microstructural gradients, which were consistent across individuals. Collectively, our findings support a common sensory-fugal axis of inter-areal cortical differentiation across histology and *in vivo* microstructure. Importantly, we observed a clear dissociation between microstructural and functional organisation that was most prominent in transmodal cortex within the default mode and fronto-parietal networks. While transmodal regions were distributed across the microstructural hierarchy, they were localised to the top of the functional hierarchy. This dissociation in transmodal regions was related to aspects of human cognition such as cognitive control and social cognition providing important support for views that these regions are relatively untethered by cortical structure and so allowing them to take on more flexible cognitive roles.

To bridge different scales of human brain organisation (50), we developed a cortico-cortical network model based on microstructural similarity between areas. Microstructure profile generation, based on state-of-the-art equivolumetric surface construction techniques (41), provided a simplified recapitulation of cellular changes across the putative laminar structure of the cortex. Importantly, our covariance framework generated cytoarchitecturally grounded networks, which were sensitive to laminar thickness as well as cell size and density. Complementing classic histological investigations that describe and delineate specific cortical areas (9–11) and more recent work identifying specific histological features of cortical areas from the BigBrain dataset (51), the current study revealed gradual cytoarchitectural transitions across the folded neocortex. Consistent with long standing views of cortical organisation from studies of non-human primates, our analysis elucidated a macroscopic

sensory-fugal axis of microstructural differentiation (52). The microstructural gradient reflected a continuum through distinct levels of laminar differentiation and cytoarchitectural complexity, from the koniocortical primary sensory areas, via unimodal association areas towards dysgranular paralimbic cortices (37,53). Notably, we could directly translate our approach to myelin sensitive *in vivo* MRI (15–19), recovering highly consistent topographic maps. Similarity of cyto- and myeloarchitectural organisation likely arises from the intrinsic relationship between horizontal axon collaterals of pyramidal neurons and myelin banding (54), and recent evidence illustrates alignment of cyto- and myeloarchitectonic layers (12).

By showing a close correlation between individualised microstructural gradients and corresponding functional connectome gradients (25), our findings expand the structural model of connectivity, initially formulated in non-human primates (14), to living humans. Microstructural and functional gradients were consistently anchored by primary sensory regions on the lower end, recapitulating their consistent location at the bottom of functional and structural hierarchies in primates (3,4,25,33,49,55). In primary regions, where neural processes are strongly constrained by sensorimotor contingencies, information processing is driven by extrinsic inputs and interactions with the outside world (56,57), as well as intrinsic signalling molecules involved in axonal guidance, cell adhesion, regional circuit formation, and thus cortical patterning (58). The impact of these forces decreases with synaptic distance, producing a sensory-fugal axis of neurostructural and functional differentiation along the cortical mantle. In fact, given the default mode network's location as the most distant functional system relative to the location of primary sensory sulci (25), it may be relatively un-tethered by the influence of intrinsic signalling molecules and extrinsic activity (59), and thus expresses less unique microstructural profiles, as observed here and in classical neuroanatomical studies (9–11). Furthermore, in contrast to a close functional coupling of microstructurally similar areas at the low end of the cortical gradient, the functional connectivity between higher-order regions may not be as strongly constrained by microstructural similarity. For example, prefrontal and parietal association regions of the higher-order networks densely interact functionally (21,23,60,61) despite distinct cytoarchitectural compositions (62). A plausible mechanism for reduced influence of microstructural homophily in higher-order networks may be the increased relevance of long-range structural connections (63). Such wider ranging structural connections may accommodate the more distributed spatial layout and diverse functional roles of transmodal cortices. Conversely, primary sensory and motor regions exhibit more locally clustered short range connectivity profiles related to microstructural similarity (64,65), likely in accordance with their more specialized and stable functional roles.

Our approach was robust with respect to variations in algorithmic and analytical choices. While the singular nature of the BigBrain dataset prohibited replication of the histological pipeline, we demonstrated consistency of neuroimaging-derived microstructural gradients across three cohorts with unique myelin sensitive contrasts (15,17,19,34,47). Importantly, the *in vivo* approach can serve as a lower resolution, yet biologically meaningful extension of the histological work. In fact, myelin-based gradients exhibited a comparable association with laminar differentiation and cytoarchitectural complexity as the histology-based gradient. With the emergence of algorithms that detect cortical laminae based on histological data (51) and increasing availability of ultra-high field MRI scanners, we expect that the histological as well as *in vivo* MPC approach may be further refined in future work, providing an even more direct bridge between the micro- and macro-scales of human brain organisation. In addition, as it offers a hierarchy-dependent reference frame to examine the interplay of microstructural and system-level network mechanisms in single individuals, the proposed framework may be advantageous in neurodevelopmental research and complement existing covariance network mapping approaches that have shown promise in studying typical and atypical development (66–71). As such, it offers a powerful and freely available (<http://github.com/micaopen/MPC>) tool to investigate coordinated changes in cortical microstructure paralleling the emergence and maturation of large-scale functional networks during development (72,73), and may conversely provide insight into the structural underpinnings of atypical network configurations in complex neurodevelopmental disorders (74).

We close by considering the significance of the observed progressive dissociation between structural and functional topographies in cortical areas involved in multi-domain, integrative processing. Components of the fronto-parietal network have been shown to guide behaviour in an adaptive

manner, changing in line with external demands (26), and possibly substantiated by its ability to dynamically reconfigure its functional connectivity (75). Although the functional role of the default mode network as the putative apex of the cortical functional hierarchy in primates remains subject to debate (76), it is evidently involved a broad class of memory-driven operations, involving self-referential and simulative thought processes and some degree of abstraction (29–31). The interesting possibility that reduced microstructural constraints enable functional diversity and flexibility was also supported by *ad hoc* meta-analytical synthesis, which suggested that structure-function decoupling preferentially related to working memory, social cognition, and cognitive control. Such a hypothesis provides a potential mechanistic account for why some of the more creative acts of the human mind emerge through the interaction of the two most dominant yet structurally diverse functional systems (77).

## ACKNOWLEDGEMENTS

Dr Paquola was funded through a postdoctoral fellowship of the Transforming Autism Care Consortium (TACC). Drs Bethlehem and Bernhardt received an MNI-Cambridge collaboration grant. Dr Bernhardt acknowledges research support from the National Science and Engineering Research Council of Canada (NSERC, Discovery-1304413), the Canadian Institutes of Health Research (CIHR, FDN-154298), the Azrieli Center for Autism Research of the Montreal Neurological Institute (ACAR), SickKids Foundation (NI17-039), and received salary support from FRQS (Chercheur Boursier Junior 1). Mr Vos de Wael was funded by a studentship of the Savoy Foundation. Dr Wagstyl was supported by the Health Brain Healthy Lives (HBHL) Initiative. Dr Bethlehem was supported by the Autism Research Trust. Mr Seidlitz was supported by the NIH-Oxford/Cambridge Scholars Program. Dr Smallwood was supported by a European Research Council Consolidator Grant (WANDERINGMINDS – 646927)

Data included in the study was provided, in part, by the Human Connectome Project, WU-Minn Consortium (Principal Investigators: David Van Essen and Kamil Ugurbil; 1U54MH091657) funded by the 16 NIH Institutes and Centers that support the NIH Blueprint for Neuroscience Research; and by the McDonnell Center for Systems Neuroscience at Washington University. An additional dataset was supported by the Neuroscience in Psychiatry Network and a strategic award by the Wellcome Trust to the University of Cambridge and University College London (095844/Z/11/Z), for which support was also provided by the National Institute for Health Research Cambridge Biomedical Research Centre and the Medical Research Council/Wellcome Trust Behavioural and Clinical Neuroscience Institute at the University of Cambridge.

The authors would also like to express their gratitude to the teams at the Forschungszentrum Julich and the Montreal Neurological Institute who made the BigBrain dataset available. Furthermore, we thank Dr Nicola Palamero-Gallagher for helpful and inspiring discussions.

## DECLARATION OF INTERESTS

Dr Bullmore is employed half-time by the University of Cambridge and half-time by GlaxoSmithKline (GSK); he holds stock in GSK. The views expressed are those of the author(s) and not necessarily those of the NHS, the NIHR, GSK or the Department of Health.



## REFERENCES

1. Petrides M. Lateral prefrontal cortex: architectonic and functional organization. *Philos Trans R Soc B Biol Sci.* 2005 Apr 29;360(1456):781–95.
2. Barbas H, Rempel-Clover N. Cortical structure predicts the pattern of corticocortical connections. *Cereb Cortex.* 1997;7(7):635–46.
3. Felleman DJ, Van Essen DC. Distributed hierarchical processing in the primate cerebral cortex. *Cereb Cortex.* 1991;1(1):1–47.
4. Mesulam M-M. From sensation to cognition. *Brain.* 1998;121:1013–52.
5. Selemon LD, Goldman-Rakic PS. Common Cortical and Subcortical Targets of the Dorsolateral Prefrontal and Posterior Parietal Cortices in the Rhesus Monkey: Evidence for a Distributed Neural Network Subserving Spatially Guided Behavior. Vol. 8, *The Journal of Neuroscience.* 1988.
6. Cavada C, Goldman-Rakic PS. Posterior parietal cortex in rhesus monkey: II. Evidence for segregated corticocortical networks linking sensory and limbic areas with the frontal lobe. *J Comp Neurol.* 1989 Sep 22;287(4):422–45.
7. Cavada C, Goldman-Rakic PS. Posterior parietal cortex in rhesus monkey: I. Parcellation of areas based on distinctive limbic and sensory corticocortical connections. *J Comp Neurol.* 1989 Sep 22;287(4):393–421.
8. Goldman-Rakic PS. Topography of Cognition: Parallel Distributed Networks in Primate Association Cortex. *Annu Rev Neurosci.* 1988;11(1):137–56.
9. Brodmann K. Vergleichende Lokalisationslehre der Grosshirnrinde in ihren Prinzipien dargestellt auf Grund des Zellenbaues. Leipzig: Barth JA; 1909.
10. Vogt C, Vogt O. Allgemeinere Ergebnisse unserer Hirnforschung. *J für Psychol und Neurol.* 1919;25(Suppl. 1):273–462.
11. Von Economo C, Koskinas G. Die Cytoarchitektonik der Hirnrinde des erwachsenen Menschen. Berlin: Springer; 1925.
12. Palomero-Gallagher N, Zilles K. Cortical layers: Cyto-, myelo-, receptor- and synaptic architecture in human cortical areas. *NeuroImage.* 2017 Aug 12;
13. Flechsig PE. Anatomie des menschlichen Gehirns und Rückenmarks auf myelogenetischer Grundlage - Paul Emil Flechsig - Google Books. Leipzig: Georg Thieme; 1920.
14. Beul SF, Barbas H, Hilgetag CC. A Predictive Structural Model of the Primate Connectome. *Sci Rep.* 2017;7.
15. Glasser MF, Van Essen DC. Mapping human cortical areas in vivo based on myelin content as revealed by T1- and T2-weighted MRI. *J Neurosci.* 2011 Aug 10;31(32):11597–616.
16. Bock NA, Kocharyan A, Liu J V., Silva AC. Visualizing the entire cortical myelination pattern in marmosets with magnetic resonance imaging. *J Neurosci Methods.* 2009 Dec 15;185(1):15–22.
17. Stüber C, Morawski M, Schäfer A, Labadie C, Wähnert M, Leuze C, et al. Myelin and iron concentration in the human brain: A quantitative study of MRI contrast. *Neuroimage.* 2014 Jun 1;93(P1):95–106.
18. Geyer S, Weiss M, Reimann K, Lohmann G, Turner R. Microstructural Parcellation of the Human Cerebral Cortex – From Brodmann’s Post-Mortem Map to in vivo Mapping with High-Field Magnetic Resonance Imaging. *Front Hum Neurosci.* 2011;5(19):1–7.
19. Schmierer K, Tozer DJ, Scaravilli F, Altmann DR, Barker GJ, Tofts PS, et al. Quantitative

- magnetization transfer imaging in postmortem multiple sclerosis brain. *J Magn Reson Imaging*. 2007 Jul;26(1):41–51.
20. Biswal B, Zerrin Yetkin F, Haughton VM, Hyde JS. Functional connectivity in the motor cortex of resting human brain using echo-planar MRI. *Magn Reson Med*. 1995;34(4):537–41.
21. Raichle ME. The brain's default mode network. *Annu Rev Neurosci*. 2015/05/06. 2015;38:433–47.
22. Smith SM, Fox PT, Miller KL, Glahn DC, Fox PM, Mackay CE, et al. Correspondence of the brain's functional architecture during activation and rest. *Proc Natl Acad Sci U S A*. 2009;106(31):13040–5.
23. Yeo BTT, Krienen FM, Sepulcre J, Thomas Yeo BT, Krienen FM, Sepulcre J, et al. The organization of the human cerebral cortex estimated by intrinsic functional connectivity. *J Neurophysiol*. 2011 Sep;106(3):1125–65.
24. Cauda F, D'Agata F, Sacco K, Duca S, Geminiani G, Vercelli A. Functional connectivity of the insula in the resting brain. *Neuroimage*. 2011 Mar 1;55(1):8–23.
25. Margulies DS, Ghosh SS, Goulas A, Falkiewicz M, Huntenburg JM, Langs G, et al. Situating the default-mode network along a principal gradient of macroscale cortical organization. *Proc Natl Acad Sci*. 2016;113(44):12574–9.
26. Duncan J. The multiple-demand (MD) system of the primate brain: mental programs for intelligent behaviour. *Trends Cogn Sci*. 2010 Apr;14(4):172–9.
27. Dosenbach NUF, Fair DA, Miezin FM, Cohen AL, Wenger KK, Dosenbach RAT, et al. Distinct brain networks for adaptive and stable task control in humans. *Proc Natl Acad Sci*. 2007 Jun 26;104(26):11073–8.
28. Corbetta M. Frontoparietal cortical networks for directing attention and the eye to visual locations: identical, independent, or overlapping neural systems? *Proc Natl Acad Sci U S A*. 1998 Feb 3;95(3):831–8.
29. Vatansever D, Menon DK, Stamatakis EA. Default mode contributions to automated information processing. *Proc Natl Acad Sci U S A*. 2017 Nov 28;114(48):12821–6.
30. Braga RM, Buckner RL. Parallel Interdigitated Distributed Networks within the Individual Estimated by Intrinsic Functional Connectivity. *Neuron*. 2017 Jul 19;95(2):457–471.e5.
31. Spreng RN, Grady CL. Patterns of Brain Activity Supporting Autobiographical Memory, Prospection, and Theory of Mind, and Their Relationship to the Default Mode Network. *J Cogn Neurosci*. 2010 Jun;22(6):1112–23.
32. Amunts K, Lepage C, Borgeat L, Mohlberg H, Dickscheid T, Rousseau M-E, et al. BigBrain: An Ultrahigh-Resolution 3D Human Brain Model. *Science (80- )*. 2013;340(6139):1472–5.
33. Sanides F. The Cyto-myeloarchitecture of the Human Frontal Lobe and its Relation to Phylogenetic Differentiation of the Cerebral Cortex. *J Hirnforsch*. 1964;6(5):269–82.
34. Van Essen DC, Smith SM, Barch DM, Behrens TEJ, Yacoub E, Ugurbil K. The WU-Minn Human Connectome Project: An overview. *Neuroimage*. 2013;80:62–79.
35. Hong S-J, Bernhardt BC, Gill RS, Bernasconi N, Bernasconi A. The spectrum of structural and functional network alterations in malformations of cortical development. *Brain*. 2017 Aug 1;140(8):2133–43.
36. Coifman RR, Lafon S, Lee AB, Maggioni M, Nadler B, Warner F, et al. Geometric diffusions as a tool for harmonic analysis and structure definition of data: Multiscale methods. *Proc Natl Acad Sci*. 2005;102(21):7432–7.

37. Mesulam M-M. Behavioral neuroanatomy: Largescale networks, association cortex, frontal syndromes, the limbic system, and hemispheric specialization. In: *Principles of Behavioral and Cognitive Neurology*. 2000. p. 1–120.
38. Vértés PE, Rittman T, Whitaker KJ, Romero-Garcia R, Váša F, Kitzbichler MG, et al. Gene transcription profiles associated with inter-modular hubs and connection distance in human functional magnetic resonance imaging networks. *Philos Trans R Soc B Biol Sci*. 2016;371(1705).
39. Burt JB, Demirtaş M, Eckner WJ, Navejar NM, Ji JL, Martin WJ, et al. Hierarchy of transcriptomic specialization across human cortex captured by structural neuroimaging topography. *Nat Neurosci*. 2018 Sep 6;21(9):1251–9.
40. Glasser MF, Sotiropoulos SN, Wilson JA, Coalson TS, Fischl B, Andersson JL, et al. The minimal preprocessing pipelines for the Human Connectome Project. *Neuroimage*. 2013 Oct 15;80:105–24.
41. Waehnert MD, Dinse J, Weiss M, Streicher MN, Waehnert P, Geyer S, et al. Anatomically motivated modeling of cortical laminae. *Neuroimage*. 2014 Jun 1;93:210–20.
42. Wagstyl K, Paquola C, Bethlehem R, Huth A. kwagstyl/surface\_tools: Initial release of equivolumetric surfaces. 2018.
43. Lewis JW, Van Essen DC. Mapping of architectonic subdivisions in the macaque monkey, with emphasis on parieto-occipital cortex. *J Comp Neurol*. 2000 Dec 4;428(1):79–111.
44. Mars RB, Passingham RE, Jbabdi S. Connectivity Fingerprints: From Areal Descriptions to Abstract Spaces. *Trends Cogn Sci*. 2018 Sep 18;22(11):1026–37.
45. Lancichinetti A, Fortunato S. Consensus clustering in complex networks. *Sci Rep*. 2012;2.
46. Goulas A, Zilles K, Hilgetag CC. Cortical Gradients and Laminar Projections in Mammals. *Trends Neurosci*. 2018 Jul 3;
47. Kiddle B, Inkster B, Prabhu G, Moutoussis M, Whitaker KJ, Bullmore ET, et al. Cohort Profile: The NSPN 2400 Cohort: a developmental sample supporting the Wellcome Trust NeuroScience in Psychiatry Network. *Int J Epidemiol*. 2018 Feb 1;47(1):18–19g.
48. Bailey P, Bonin G von. *The isocortex of man*. Urbana: University of Illinois Press; 1951.
49. Fulcher BD, Murray JD, Zerbi V, Wang X-J. Multimodal gradients across mouse cortex.
50. van den Heuvel MP, Yeo BTT. A Spotlight on Bridging Microscale and Macroscale Human Brain Architecture. Vol. 93, *Neuron*. 2017. p. 1248–51.
51. Wagstyl K, Lepage C, Bludau S, Zilles K, Fletcher PC, Amunts K, et al. Mapping Cortical Laminar Structure in the 3D BigBrain. *Cereb Cortex*. 2018 Jul 1;28(7):2551–62.
52. Von Bonin G, Bailey P. *The neocortex of Macaca mulatta*. University of Illinois Press. 1947.
53. Sanides F. Functional Architecture of Motor and Sensory Cortices in Primates in the Light of a New Concept of Neocortex Evolution \*. In: Noback CR, Montagna W, editors. *The Primate Brain*. New York: Appleton-Century-Crofts; 1970. p. 136–208.
54. Hellwig B. How the myelin picture of the human cerebral cortex can be computed from cytoarchitectural data. A bridge between von Economo and Vogt. *J Hirnforsch*. 1993;34(3):387–402.
55. Huntenburg JM, Bazin PL, Goulas A, Tardif CL, Villringer A, Margulies DS. A Systematic Relationship Between Functional Connectivity and Intracortical Myelin in the Human Cerebral Cortex. *Cereb Cortex*. 2017;27(2):981–97.
56. Rakic P. Specification of cerebral cortical areas. *Science* (80- ). 1988;241(4862):170–6.



57. O’Leary DDM, Chou S-J, Sahara S. Area Patterning of the Mammalian Cortex. *Neuron*. 2007 Oct 25;56(2):252–69.
58. Fukuchi-Shimogori T, Grove EA. Neocortex patterning by the secreted signaling molecule FGF8. *Science* (80- ). 2001;294(5544):1071–4.
59. Buckner RL, Krienen FM. The evolution of distributed association networks in the human brain. Vol. 17, *Trends in Cognitive Sciences*. 2013. p. 648–65.
60. Harding IH, Yücel M, Harrison BJ, Pantelis C, Breakspear M. Effective connectivity within the frontoparietal control network differentiates cognitive control and working memory. *Neuroimage*. 2015 Feb 1;106:144–53.
61. Shulman GL, Fiez JA, Corbetta M, Buckner RL, Miezin FM, Raichle ME, et al. Common Blood Flow Changes across Visual Tasks: II. Decreases in Cerebral Cortex. *J Cogn Neurosci*. 1997 Oct 7;9(5):648–63.
62. Solari SVH, Stoner R. Cognitive consilience: primate non-primary neuroanatomical circuits underlying cognition. *Front Neuroanat*. 2011;5:65.
63. Hagmann P, Cammoun L, Gigandet X, Meuli R, Honey CJ, Van Waden J, et al. Mapping the structural core of human cerebral cortex. *PLoS Biol*. 2008 Jul 1;6(7):1479–93.
64. Oligschläger S, Huntenburg JM, Golchert J, Lauckner ME, Bonnen T, Margulies DS. Gradients of connectivity distance are anchored in primary cortex. *Brain Struct Funct*. 2017 Jul;222(5):2173–82.
65. Sepulcre J, Liu H, Talukdar T, Martincorena I, Thomas Yeo BT, Buckner RL. The organization of local and distant functional connectivity in the human brain. *Sporns O, editor. PLoS Comput Biol*. 2010 Jun 10;6(6):1–15.
66. Alexander-Bloch A, Raznahan A, Bullmore E, Giedd J. The Convergence of Maturation Change and Structural Covariance in Human Cortical Networks. *J Neurosci*. 2013;33(7):2889–99.
67. Zielinski BA, Gennatas ED, Zhou J, Seeley WW. Network-level structural covariance in the developing brain. *Proc Natl Acad Sci U S A*. 2010;107(42):18191–6.
68. Bonilha L, Tabesh A, Dabbs K, Hsu DA, Stafstrom CE, Hermann BP, et al. Neurodevelopmental alterations of large-scale structural networks in children with new-onset epilepsy. *Hum Brain Mapp*. 2014 Aug;35(8):3661–72.
69. Palaniyappan L, Park B, Balain V, Dangi R, Liddle P. Abnormalities in structural covariance of cortical gyrification in schizophrenia. *Brain Struct Funct*. 2015 Jul 26;220(4):2059–71.
70. Bethlehem RAI, Romero-Garcia R, Mak E, Bullmore ET, Baron-Cohen S. Structural Covariance Networks in Children with Autism or ADHD. *Cereb Cortex*. 2017 Aug 1;27(8):4267–76.
71. Seidlitz J, Váša F, Shinn M, Romero-Garcia R, Whitaker KJ, Vértes PE, et al. Morphometric Similarity Networks Detect Microscale Cortical Organization and Predict Inter-Individual Cognitive Variation. *Neuron*. 2018;97(1):231–247.e7.
72. Whitaker KJ, Vértes PE, Romero-Garcia R, Váša F, Moutoussis M, Prabhu G, et al. Adolescence is associated with genomically patterned consolidation of the hubs of the human brain connectome. *Proc Natl Acad Sci*. 2016 Aug 9;113(32):9105–10.
73. Grydeland H, Walhovd KB, Tamnes CK, Westlye LT, Fjell AM. Intracortical Myelin Links with Performance Variability across the Human Lifespan: Results from T1- and T2-Weighted MRI Myelin Mapping and Diffusion Tensor Imaging. *J Neurosci*. 2013;33(47):18618–30.

74. DiMartino A, Fair DA, Kelly C, Satterthwaite TD, Castellanos FX, Thomason ME, et al. Unraveling the miswired connectome: A developmental perspective. Vol. 83, *Neuron*. 2014. p. 1335–53.
75. Cole MW, Reynolds JR, Power JD, Repovs G, Anticevic A, Braver TS. Multi-task connectivity reveals flexible hubs for adaptive task control. *Nat Neurosci*. 2013 Sep 28;16(9):1348–55.
76. Buckner RL, Margulies DS. Macroscale Cortical Organization and a Default-Like Transmodal Apex Network in the Marmoset Monkey. *bioRxiv*. 2018 Sep 12;415141.
77. Beaty RE, Kenett YN, Christensen AP, Rosenberg MD, Benedek M, Chen Q, et al. Robust prediction of individual creative ability from brain functional connectivity. *Proc Natl Acad Sci U S A*. 2018 Jan 30;115(5):1087–92.
78. Merker B. Silver staining of cell bodies by means of physical development. *J Neurosci Methods*. 1983;9(3):235–41.
79. Lepage C, Mohlberg H, Pietrzyk U, Amunts K, Zilles K, Evans A. Automatic repair of acquisition defects in reconstruction of histology slices of the human brain. In: 16th Annual Meeting of the Organization for Human Brain Mapping (OHBM). Barcelona; 2010.
80. Mohlberg H, Tweddell B, Lippert T, Amunts K. Workflows for Ultra-High Resolution 3D Models of the Human Brain on Massively Parallel Supercomputers. In Springer, Cham; 2016. p. 15–27.
81. Lewis LB, Lepage C, Marc F, Zilles K, Amunts K, Evans AC. BigBrain: Initial Tissue Classification and Surface Extraction. In: Organisation for Human Brain Mapping. Hamburg; 2014.
82. Worsley K, Taylor J, Carbonell F, Chung M, Duerden E, Bernhardt B, et al. SurfStat: A Matlab toolbox for the statistical analysis of univariate and multivariate surface and volumetric data using linear mixed effects models and random field theory. In: Human Brain Mapping. 2009.
83. Lange T, Roth V, Braun ML, Buhmann JM. Stability-Based Validation of Clustering Solutions. *Neural Comput*. 2004;16(6):1299–323.
84. Vos de Wael R, Larivière S, Caldairou B, Hong S-J, Margulies DS, Jefferies E, et al. Anatomical and microstructural determinants of hippocampal subfield functional connectome embedding. *Proc Natl Acad Sci U S A*. 2018 Sep 24;115(40):10154–9.
85. Von Luxburg U. A tutorial on spectral clustering. *Stat Comput*. 2007 Dec 22;17(4):395–416.
86. Tenenbaum JB, De Silva V, Langford JC. A global geometric framework for nonlinear dimensionality reduction. *Science* (80- ). 2000 Dec 22;290(5500):2319–23.
87. Glasser MF, Coalson TS, Robinson EC, Hacker CD, Harwell J, Yacoub E, et al. A multi-modal parcellation of human cerebral cortex. *Nature*. 2016;536(7615):171–8.
88. Smith SM, Beckmann CF, Andersson J, Auerbach EJ, Bijsterbosch J, Douaud G, et al. Resting-state fMRI in the Human Connectome Project. *Neuroimage*. 2013;80:144–68.
89. Sled JGG, Zijdenbos APP, Evans ACC. A nonparametric method for automatic correction of intensity nonuniformity in MRI data. *IEEE Trans Med Imaging*. 1998 Feb;17(1):87–97.
90. Fischl B, Sereno MI, Dale AM. Cortical surface-based analysis. II: Inflation, flattening, and a surface-based coordinate system. *Neuroimage*. 1999/02/05. 1999;9(2):195–207.
91. Dale AM, Fischl B, Sereno MI. Cortical surface-based analysis. I. Segmentation and surface reconstruction. *Neuroimage*. 1999;9(2):179–94.

92. Fischl B, Sereno MI, Tootell RB, Dale AM. High-resolution intersubject averaging and a coordinate system for the cortical surface. *Hum Brain Mapp.* 2000/01/05. 1999;8(4):272–84.
93. Robinson EC, Jbabdi S, Glasser MF, Andersson J, Burgess GC, Harms MP, et al. MSM: A new flexible framework for multimodal surface matching. *Neuroimage.* 2014;100:414–26.
94. Robinson EC, Garcia K, Glasser MF, Chen Z, Coalson TS, Makropoulos A, et al. Multimodal surface matching with higher-order smoothness constraints. *Neuroimage.* 2018;167:453–65.
95. Van Essen DC, Glasser MF, Dierker DL, Harwell J, Coalson T. Parcellations and hemispheric asymmetries of human cerebral cortex analyzed on surface-based atlases. *Cereb Cortex.* 2012;22(10):2241–62.
96. Greve DN, Fischl B. Accurate and robust brain image alignment using boundary-based registration. *Neuroimage.* 2009;48(1):63–72.
97. Salimi-Khorshidi G, Douaud G, Beckmann CF, Glasser MF, Griffanti L, Smith SM. Automatic denoising of functional MRI data: Combining independent component analysis and hierarchical fusion of classifiers. *Neuroimage.* 2014;90:449–68.
98. Murphy K, Fox MD. Towards a consensus regarding global signal regression for resting state functional connectivity MRI. *Neuroimage.* 2017 Jul 1;154:169–73.
99. Vos de Wael R, Hyder F, Thompson GJ. Effects of Tissue-Specific Functional Magnetic Resonance Imaging Signal Regression on Resting-State Functional Connectivity. *Brain Connect.* 2017;7(8):482–90.
100. Yarkoni T, Poldrack RA, Nichols TE, Van Essen DC, Wager TD. Large-scale automated synthesis of human functional neuroimaging data. *Nat Methods.* 2011 Aug 26;8(8):665–70.
101. Marques JP, Kober T, Krueger G, van der Zwaag W, Van de Moortele P-FF, Gruetter R. MP2RAGE, a self bias-field corrected sequence for improved segmentation and T1-mapping at high field. *Neuroimage.* 2010 Jan 15;49(2):1271–81.
102. Haast RAM, Ivanov D, Formisano E, Uludağ K. Reproducibility and Reliability of Quantitative and Weighted T1 and T2\* Mapping for Myelin-Based Cortical Parcellation at 7 Tesla. *Front Neuroanat.* 2016;10:112.



## MATERIALS AND METHODS

### Histology-based MPC

#### *Histological data acquisition and preprocessing*

An ultra-high resolution Merker stained 3D volumetric histological reconstruction of a *post mortem* human brain from a 65-year-old male was obtained from the open-access BigBrain repository on February 2, 2018 [<https://bigbrain.loris.ca/main.php>; (32)]. The *post mortem* brain was paraffin-embedded, coronally sliced into 7,400 20µm sections, silver-stained for cell bodies (78) and digitised. Manual inspection for artefacts (*i.e.*, rips, tears, shears, and stain crystallisation) was followed by automatic repair procedures, involving non-linear alignment to a *post mortem* MRI, intensity normalisation, and block averaging (79). 3D reconstruction was implemented with a successive coarse-to-fine hierarchical procedure (80). We downloaded the 3D volume at four resolutions, with 100, 200, 300, and 400µm isovoxel size. We primarily analysed 100µm data and used 200, 300 and 400µm data to assess consistency of findings across spatial scales. Computations were performed on inverted images, where staining intensity reflects cellular density and soma size. Geometric meshes approximating the outer and inner cortical interface (*i.e.*, the GM/CSF boundary and the GM/WM boundary) with 163,842 matched vertices per hemisphere were also available (81).

#### *Histology-based microstructure profile covariance (MPC) analysis*

*a) Surface sampling.* We systematically constructed 10-100 equivolumetric surfaces, in steps of 1, between the outer and inner cortical surfaces (42). The equivolumetric model compensates for cortical folding by varying the Euclidean distance,  $\rho$ , between pairs of intracortical surfaces throughout the cortex to preserve the fractional volume between surfaces (41).  $\rho$  was calculated as follows for each surface

$$\rho = \frac{1}{A_{out} - A_{in}} \cdot (-A_{in} + \sqrt{\alpha A_{out}^2 + (1 - \alpha) A_{in}^2}) \quad (1)$$

where  $\alpha$  represents fraction of the total volume of the segment accounted for by the surface, while  $A_{out}$  and  $A_{in}$  represent the surface area of the outer and inner cortical surfaces, respectively. Next, vertex-wise microstructure profiles were estimated by sampling intensities along linked vertices from the outer to the inner surface across the whole cortex. In line with previous work (51), layer 1 was approximated as the top ten percent of surfaces and removed from the analysis due to little inter-regional variability. Note however, that findings were nevertheless virtually identical when keeping the top ten percent of surfaces. To reduce the impact of partial volume effects, the deepest surface was also removed. Surface-based linear models, implemented via SurfStat for Matlab (<http://www.math.mcgill.ca/keith/surfstat/>) (82), were used to account for an anterior-posterior increase in intensity values across the BigBrain due to coronal slicing and reconstruction (32), whereby standardised residuals from a simple linear model of surface-wide intensity values predicted by the midsurface y-coordinate were used in further analyses.

*b) MPC matrix construction.* Cortical vertices were parcellated into 1,012 spatially contiguous cortical ‘nodes’ of approximately 1.5cm<sup>2</sup> surface area, excluding outlier vertices with median intensities more than three scaled median absolute deviations away from the node median intensity. The parcellation scheme preserves the boundaries of the Desikan Killany atlas (35) and was transformed from conte69 surface to the BigBrain midsurface via nearest neighbour interpolation. Nodal intensity profiles underwent pairwise Pearson product-moment correlations, controlling for the average whole-cortex intensity profile. MPC<sub>HIST</sub> for a given pair of nodes  $i$  and  $j$  was thus

$$\text{MPC}_{\text{HIST}}(i,j) = \frac{r_{ij} - r_{ic}r_{jc}}{\sqrt{(1 - r_{ic}^2)(1 - r_{jc}^2)}} \quad (2)$$

where  $r_{ij}$  is the Pearson product moment correlation coefficient of the BigBrain intensity profiles at nodes  $i$  and  $j$ ,  $r_{ic}$  the correlation coefficient of the intensity profile at node  $i$  with the average intensity profile across the entire cortex, and  $r_{jc}$  the Pearson correlation of the intensity profile at node  $j$  with the average intensity profile across the whole brain. The MPC matrix was absolutely thresholded at

zero then remaining MPC values were log-transformed to produce a symmetric  $1012 \times 1012$  MPC<sub>HIST</sub> matrix. The in-house developed code for MPC construction is available online (<https://github.com/MICA-MNI/micaopen/MPC>).

*c) Parameter estimation.* The optimal surface number was determined based on the stability of the MPC matrix. This procedure involved (repeatedly and randomly) dividing the vertex intensity profiles within each node into two groups and constructing two MPC matrices, then calculating the Euclidean distance between them. The procedure was repeated 1000 times. Although the MPC matrix instability was robust to variations in surface number, the 18-surface solution exhibited a noticeable local minimum MPC instability in the studied range (10-100 surfaces) and was used in subsequent analyses (SI FIGURE S2). Notably, the MPC gradient was similar using two finer grained solutions (i.e., 54 and 91 surfaces), where local minima were observed as well. More details on the origins of the stability statistic in clustering algorithms may be found elsewhere (83).

*d) Relation to spatial proximity.* To determine whether MPC<sub>HIST</sub> was not purely driven by spatial proximity, we correlated MPC<sub>HIST</sub> strength with geodesic distance for all node pairs. The latter was calculated using the Fast Marching Toolbox between all pairs of vertices, then averaged by node (<https://github.com/gpeyre/matlab-toolboxes/tree/master/>).

### *Histology-based MPC gradient mapping*

In line with previous studies (25,84), the MPC<sub>HIST</sub> matrix was proportionally thresholded at 90% per row, then converted into a normalised angle matrix. We then applied diffusion map embedding (36), a nonlinear manifold learning technique, to identify principal gradient components explaining MPC<sub>HIST</sub> variance in descending order (each of  $1 \times 1012$ ). In brief, the algorithm estimates a low-dimensional embedding from a high-dimensional affinity matrix. In this space, cortical nodes that are strongly inter-connected by either many suprathreshold edges or few very strong edges are closer together, whereas nodes with little or no inter-covariance are farther apart. The name of this approach, which belongs to the family of graph Laplacians, derives from the equivalence of the Euclidean distance between points in the embedded space and the diffusion distance between probability distributions centred at those points. Compared to other non-linear manifold learning techniques, the diffusion maps algorithm is relatively robust to noise and computationally inexpensive (85,86). Notably, the algorithm is controlled by a single parameter  $\alpha$ , which controls the influence of the density of sampling points on the manifold ( $\alpha = 0$ , maximal influence;  $\alpha = 1$ , no influence). In this and previous studies (25,84), we followed previous recommendations and set  $\alpha=0.5$ , a choice that retains the global relations between data points in the embedded space and has been suggested to be relatively robust to noise in the covariance matrix. Gradients were mapped back onto BigBrain midsurface and visualised with SurfStat for Matlab (<http://www.math.mcgill.ca/keith/surfstat/>) (82), and we assessed the amount of MPC<sub>HIST</sub> variance explained. To show how the principal gradient in MPC<sub>HIST</sub> ( $G1_{HIST}$ ) relates to systematic variations in microstructure, we calculated and plotted the mean microstructure profiles within ten equally-sized discrete bins of  $G1_{HIST}$ .

### *Relation of $G1_{HIST}$ to laminar differentiation and cytoarchitectural taxonomy*

We evaluated correspondence of  $G1_{HIST}$  to atlas information on laminar differentiation and cytoarchitectural class. To this end, each cortical node was assigned to one of four levels of laminar differentiation (i.e., idiotypic, unimodal, heteromodal or paralimbic) derived from a seminal model of Mesulam, which was built on the integration of neuroanatomical, electrophysiological, and behavioural studies in human and non-human primates (37), and one of the seven Von Economo/Koskinas cytoarchitectural classes (i.e., primary sensory, secondary sensory, motor, association 1, association 2, limbic or insular) (11,38). In the case of laminar differentiation maps, assignment was done manually; in the case of cytoarchitectural classes, we mapped previously published Von Economo/Koskinas classes (71) to the BigBrain midsurface with nearest neighbour interpolation and assigned nodes to the cytoarchitectural class most often represented by the underlying vertices. Finally, we estimated the contribution of level of laminar differentiation (D, a

categorical variable) and cytoarchitectural class (C, a categorical variable) to the principal gradient  $G1_{\text{HIST}}$  of the  $\text{MPC}_{\text{HIST}}$  within two separate multiple regression models:

$$G1_{\text{HIST}} \sim \beta_0 + \beta_1 D + \varepsilon \quad (3)$$

$$G1_{\text{HIST}} \sim \beta_0 + \beta_1 C + \varepsilon \quad (4)$$

We evaluated the model fit via adjusted  $R^2$  statistics and unique variances explained by each predictor ( $\beta$ ).

## In vivo MPC

### *MRI data acquisition and preprocessing*

We studied data from 219 unrelated healthy adults from the minimally preprocessed S900 release of the Human Connectome Project (HCP; Glasser *et al.*, 2013). The *Discovery* dataset included 110 individuals (66 females, mean $\pm$ SD age=28.8 $\pm$ 3.8 years) and the *Replication* dataset 109 (62 females, mean $\pm$ SD age=28.5 $\pm$ 3.7 years). MRI data were acquired on the HCP's custom 3T Siemens Skyra equipped with a 32 channel head coil. Two T1w images with identical parameters were acquired using a 3D-MPRAGE sequence (0.7mm isotropic voxels, matrix=320 $\times$ 320, 256 sagittal slices; TR=2400ms, TE=2.14ms, TI=1000ms, flip angle=8 $^\circ$ ; iPAT=2). Two T2w images were acquired using a 3D T2-SPACE sequence with identical geometry (TR=3200ms, TE=565ms, variable flip angle; iPAT=2). Four rs-fMRI scans were acquired using multi-band accelerated 2D-BOLD echo-planar imaging (2mm isotropic voxels, matrix=104 $\times$ 90, 72 sagittal slices; TR=720ms, TE=33ms, flip angle=52 $^\circ$ ; mb factor=8; 1200 volumes/scan). Subjects were instructed to keep their eyes open, look at fixation cross, and not fall asleep. While T1w and T2w scans were acquired on the same day, rs-fMRI scans were split over two days (two scans/day).

Structural and resting state functional MRI data underwent HCP's minimal preprocessing (40,87,88). For structural MRI, images underwent gradient nonlinearity correction. When repeated scans were available, these were co-registered and averaged. Following brain extraction and readout distortion correction, T1w and T2w images were co-registered using rigid body transformations. Subsequently, non-uniformity correction using T1w and T2w contrast was applied (89). Preprocessed images were nonlinearly registered to MNI152 space and cortical surfaces were extracted using FreeSurfer 5.3.0-HCP (90–92), with minor modifications to incorporate both T1w and T2w (15). Cortical surfaces in individual subjects were aligned using MSMAll (93,94) to the hemisphere-matched conte69 template (95). T1w images were divided by aligned T2w images to produce a single volumetric T1w/T2w image per subject (Glasser and Van Essen, 2011). Notably, this contrast nullifies inhomogeneities related to receiver coils and increases sensitivity to intracortical myelin.

For resting state functional MRI, the timeseries were corrected for gradient nonlinearity and head motion. The R-L/L-R blipped scan pairs were used to correct for geometric distortions. Distortion corrected images were warped to T1w space using a combination of rigid body and boundary-based registrations (96). These transformations were concatenated with the transformation from native T1w to MNI152, to warp functional images to MNI152. Further processing removed the bias field (as calculated for the structural image), extracted the brain, and normalised whole brain intensity. A high-pass filter (>2000s FWHM) corrected the time series for scanner drifts, and additional noise was removed using ICA-FIX (97). Tissue-specific signal regression was not performed (98,99). Following the minimal preprocessing pipeline, we transformed resting state functional MRI to native space and sampled time-series at each vertex of the MSMAll-registered (93,94) mid-thickness cortical surfaces.

### *In vivo microstructure profile covariance (MPC) analysis*

We estimated MPC in the *in vivo* dataset ( $\text{MPC}_{\text{MRI}}$ ) in the same manner as  $\text{MPC}_{\text{HIST}}$  with the only adjustment that intensity profiles were not corrected for y-coordinates; instead, the contrast reversal for T1w and T2w data was used to correct for inhomogeneity as part of the minimal processing pipeline of the Human Connectome Project. We generated equivolumetric surfaces between the outer



and inner cortical surfaces (see Equation (1)), and systematically sampled T1w/T2w values along 64,984 linked vertices from the outer to the inner surface across the whole cortex. In turn,  $MPC_{MRI}$  can be denoted as an extension of Equation (2), in which  $MPC_{MRI}(i,j)$  for a given pair of nodes  $i$  and  $j$  is defined by:

$$MPC_{MRI}(i,j) = \frac{1}{n} \sum_{s=1}^n \left( \frac{r_{ij} - r_{ic} r_{jc}}{\sqrt{(1 - r_{ic}^2)(1 - r_{jc}^2)}} \right)_s \quad (5)$$

where  $s$  is a subject and  $n$  is the number of subjects. We systematically evaluated matrix stability across different intracortical surface numbers and selected the most stable solution (**SI FIGURE S8**).

#### *In vivo MPC<sub>MRI</sub> gradient: relation to the sensory-fugal gradient and the histological MPC gradient*

As for the histological data, diffusion map embedding derived a principal gradient ( $G1_{MRI}$ ) from the group average  $MPC_{MRI}$  matrix. Correspondence of the *in vivo*  $G1_{MRI}$  to the histological  $G1_{HIST}$  gradient was estimated via Spearman rank correlation between spatially matched nodes. To localise differences, we calculated the difference in rank of each node. As before, we assessed the contribution of level of laminar differentiation and cytoarchitectural class to the  $G1_{MRI}$  via multiple regression.

#### **Correspondence of microstructure and functional connectivity**

Individual functional connectomes were generated by averaging preprocessed timeseries within nodes, correlating nodal timeseries and converting them to z scores. For each individual, the four available resting state scans were averaged at the matrix level. Then, a group average functional connectome was calculated across the *Discovery* cohort. Correlation coefficients were calculated between the group average functional connectome and the  $MPC_{HIST}$  and  $MPC_{MRI}$  matrices. The group average functional connectome was proportionally thresholded at 90% per row, transformed into a cosine similarity matrix, transformed into a normalised angle matrix, then diffusion map embedding was applied, producing  $G1_{FUNC}$ . We calculated the correspondence of the  $G1_{FUNC}$  with  $G1_{HIST}$  and  $G1_{MRI}$  with Spearman rank correlations. The differences in the gradients were localised by comparing node ranks across the whole cortex and within functional communities. Seven functional communities were mapped onto the conte69 surfaces from a previously published parcellation (23) with nearest neighbour interpolation from fsaverage5, then nodes were assigned to the functional community most often represented by the underlying vertices. To aid interpretation of the modality-specific gradients,  $G1_{MRI}$  and  $G1_{FUNC}$  were discretised into fifty equally sized bins and we calculated the proportion of each bin accounted for by each functional community, then performed seven paired t-tests contrasting average node rank of a functional community in  $G1_{MRI}$  and  $G1_{FUNC}$  across individuals.

We used the NeuroSynth meta-analytic database ([www.neurosynth.org](http://www.neurosynth.org)) (100) to assess which cognitive functions were associated with shifts between  $G1_{MRI}$  and  $G1_{FUNC}$ . To this end, we downloaded and surface projected meta-analytic z-statistic maps of 24 terms covering a wide range of cognitive functions, which correspond to the topic names defined by Margulies *et al.*, (2016). We discretised  $G1_{MRI}$  and  $G1_{FUNC}$  into five-percentile bins and, for each term, calculated the mean z-statistic within each bin. From this, we deduced the centre of gravity of each term within gradient space, and contrasted the term-specific centre of gravity in  $G1_{MRI}$  and  $G1_{FUNC}$  at an individual level.

#### **Robustness of the MPC approach**

##### *Individualised MPC<sub>MRI</sub> gradients and relation to the individual-specific functional hierarchy*

Inter-individual consistency of  $G1_{MRI}$  was assessed in the *Replication* dataset. The  $MPC_{MRI}$  pipeline was deployed at an individual level, thus resolving individualised  $MPC_{MRI}$  matrices and gradients. Additionally, the diffusion map embedding was employed on functional connectomes to derive individual functional gradients (25). To ensure the spatial correspondence of individual gradients, the individual gradients from the *Replication* dataset underwent Procrustes linear alignment to the

*Discovery* dataset group average embedding. Individual cross-modal coupling was calculated as the Spearman rank correlation between  $G1_{MRI}$  and  $G1_{FUNC}$ .

### *Robustness of $G1_{HIST}$*

We assessed the robustness of  $G1_{HIST}$  by altering pipeline parameters, repeating  $MPC_{HIST}$  generation and diffusion map embedding, then calculating the Pearson correlation of the modified  $G1_{HIST}$  with the original gradient. In particular, we evaluated variable matrix thresholds (*i.e.*, 70-95%, in steps of 1%), alternative surface number in which  $MPC_{HIST}$  matrix instability reached a local minima (*i.e.*, 54- and 91-surface solutions), the voxel resolution of the BigBrain volume (100-400  $\mu m$ ), and spatial scale (*i.e.*, vertex- vs parcel wise construction); for the latter, we correlated nodal gradient values with the median vertex within each parcel.

### *Robustness of $G1_{MRI}$*

We repeated the robustness procedures reported for the histological gradients in the *in vivo* dataset, including variation of thresholding level, parcellation usage and surface number. Here, the pipeline was repeated with 23 surfaces, pertaining to local minima in the *in vivo*  $MPC_{MRI}$  matrix instability.

### *Independent replications of $G1_{MRI}$*

We replicated the *in vivo* gradient in two independent datasets, based on two additional myelin sensitive magnetic resonance imaging contrasts.

a) *Quantitative T1*. We implemented the MPC approach on 17 healthy adults (5 females, mean $\pm$ SD age=28.1 $\pm$ 6.1, 2 left handed) for whom quantitative T1 relaxation time mapping (qT1) images were available. All participants gave informed consent and the study was approved by the local research ethics board of the Montreal Neurological Institute and Hospital. MRI data was acquired on a 3T Siemens Magnetom Prisma-Fit with a 64-channel head coil. A submillimetric T1-weighted image was acquired using a 3D-MPRAGE sequence (0.8mm isotropic voxels, 320x320 matrix, 24 sagittal slices, TR=2300ms, TE=3.14ms, TI=900ms, flip angle=9°, iPAT=2) and qT1 data was acquired using a 3D-MP2RAGE sequence (0.8mm isotropic voxels, 240 sagittal slices, TR=5000ms, TE=2.9ms, TI 1=940ms, TI 2=2830ms, flip angle 1=4°, flip angle 2=5°, iPAT=3, bandwidth = 270 Hz/px, echo spacing = 7.2ms, partial Fourier = 6/8). The combination of two inversion images in qT1 mapping minimises sensitivity to B1 inhomogeneities (101), and provides high intra-subject and inter-subject reliability (102).

Cortical surfaces were extracted from the T1-weighted scans using FreeSurfer 6.0 (90–92), and fourteen equivolumetric intracortical surfaces were generated (42). qT1 was registered to Freesurfer native space using a boundary-based registration (96), and Freesurfer native space was registered to standard conte69 space using Caret5 landmark-based registration (95). We used the former to sample qT1 intensity values along the intracortical surfaces, and the latter to resample the evaluated surfaces to a common conte69 space with 64,984 matched vertices. As in the main approach, we averaged vertex-wise intensity profiles within 1012 nodes (35), computed pairwise partial correlations between nodal intensity profiles (controlling for the average intensity profile), kept only positive correlations, and log-transformed the result to produce a  $MPC_{MRI-QT1}$  matrix. Finally, we generated a group-average  $MPC_{MRI-QT1}$  matrix and applied diffusion map embedding. The similarity of  $G1_{MRI-QT1}$  to the original  $G1_{MRI}$  was measured with a node-wise Spearman rank correlation.

b) *Magnetisation transfer*. In an open dataset of 297 healthy young adults (149 female, mean $\pm$ SD age=19.1 $\pm$ 2.9; Kiddle *et al.*, 2018), we studied intracortical depth profiles of magnetisation transfer (MT). MT is a validated measure of myelination (19), and was available in the form of average intensity values along eight equidistant intracortical surfaces (10% - 90% in 10% intervals) within 308 cortical regions (for further details see (72)). We similarly applied the MPC framework to the MT profiles, then averaged the  $MPC_{MRI-MT}$  matrix across the group and applied diffusion map embedding. We measured the Spearman rank correlation between  $G1_{MRI-MT}$  and the original  $G1_{MRI}$ , which was recalculated with 308 matched cortical areas.

# DISSOCIATIONS BETWEEN MICROSTRUCTURAL AND FUNCTIONAL HIERARCHIES WITHIN REGIONS OF TRANSMODAL CORTEX

PAQUOLA C<sup>1</sup>, VOS DE WAELE R<sup>1</sup>, WAGSTYL K<sup>2</sup>, BETHLEHEM RAI<sup>3</sup>, HONG SJ<sup>1</sup>, SEIDLITZ J<sup>4,5</sup>, BULLMORE ET<sup>5</sup>, EVANS AC<sup>1,2</sup>, MISIC B<sup>1</sup>, MARGULIES DS<sup>6</sup>, SMALLWOOD J<sup>7</sup>,  
BERNHARDT BC<sup>1\*</sup>

<sup>1</sup> McConnell Brain Imaging Centre, Montreal Neurological Institute and Hospital, McGill University, Montreal, QC, Canada; <sup>2</sup> McGill Centre for Integrative Neuroscience, McGill University, Montreal, QC, Canada; <sup>3</sup> Autism Research Centre, Department of Psychiatry, University of Cambridge, England, United Kingdom; <sup>4</sup> Developmental Neurogenetics Unit, National Institute of Mental Health, Bethesda, MD 20892, USA; <sup>5</sup> Brain Mapping Unit, University of Cambridge, Department of Psychiatry, Cambridge CB2 0SZ, UK; <sup>6</sup> Frontlab, Institut du Cerveau et de la Moelle épinière, UPMC UMRS 1127, Inserm U 1127, CNRS UMR 7225, Paris, France; <sup>7</sup> York Neuroimaging Center, University of York, UK

## SUPPLEMENTAL INFORMATION:

**FIGURE S1-11**

**TABLE S1-5**

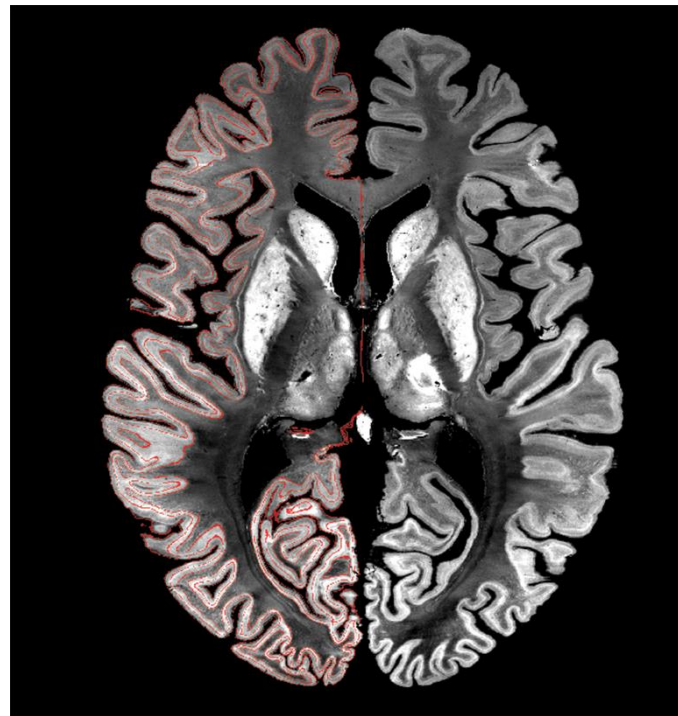


**FIGURE S1.** Horizontal view of the volumetric reconstruction of the “BigBrain” with pial, mid and white matter surfaces projected on the left hemisphere. Notably, we corrected for the linear relationship between intensity values and midsurface y-coordinate ( $r=-0.68$ ,  $p<0.001$ ), which existed due to coronal slicing and reconstruction of the BigBrain.



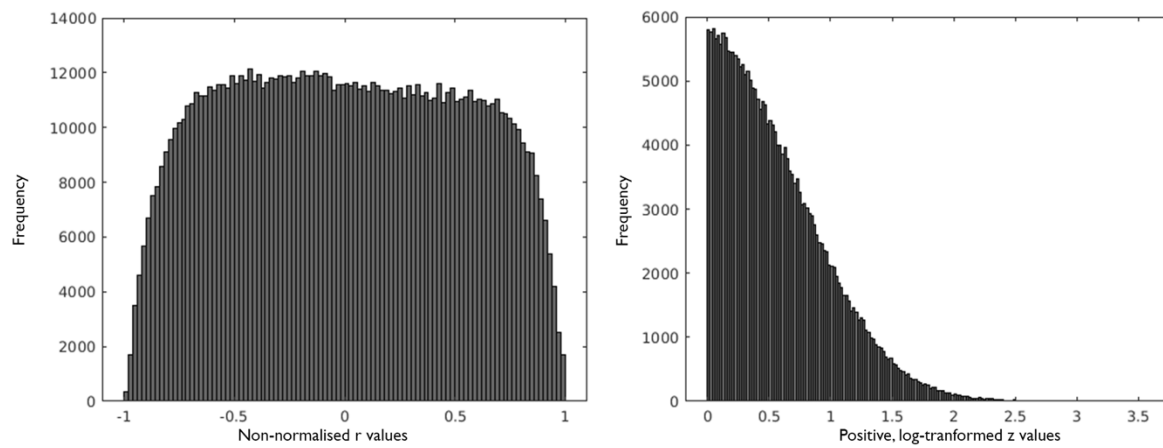


**FIGURE S2.** Distribution of values in MPC<sub>HIST</sub> matrix. (*Left*) Frequency of  $r$  values calculated by Pearson product moment correlation coefficient of the nodal intensity profiles, controlling for the average intensity profile. (*Right*) Frequency of positive  $z$  values following log transformation of  $r$  values.

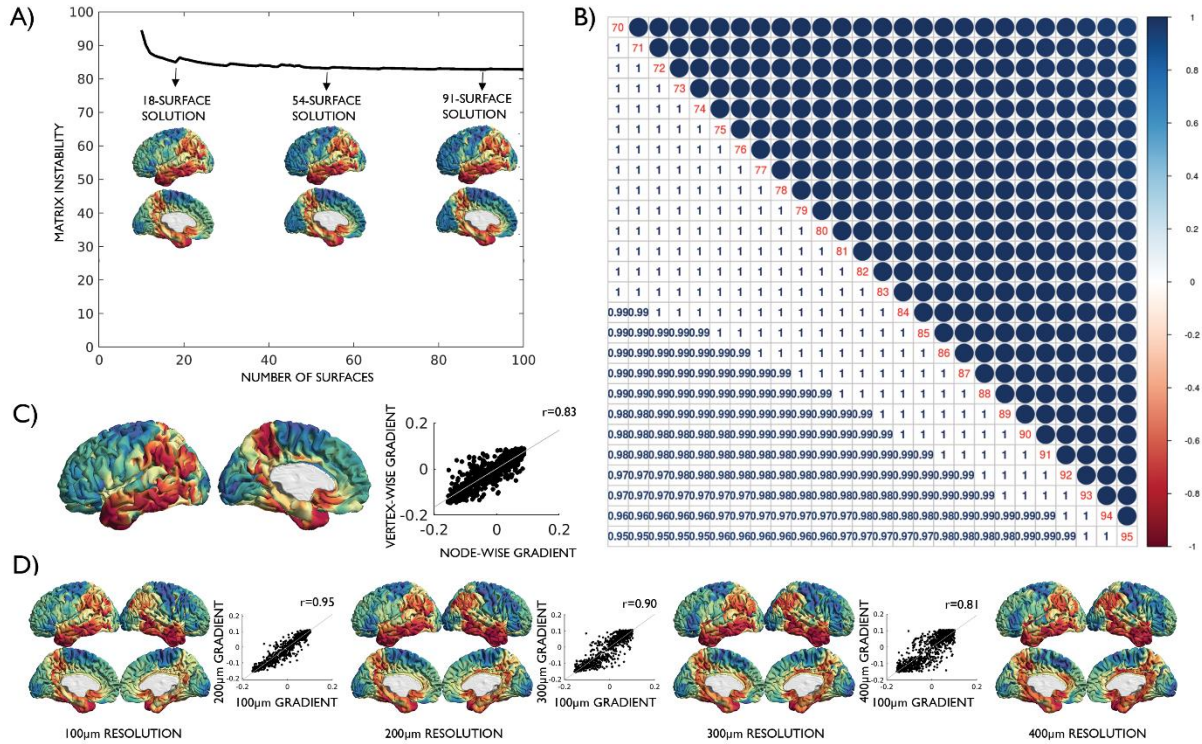
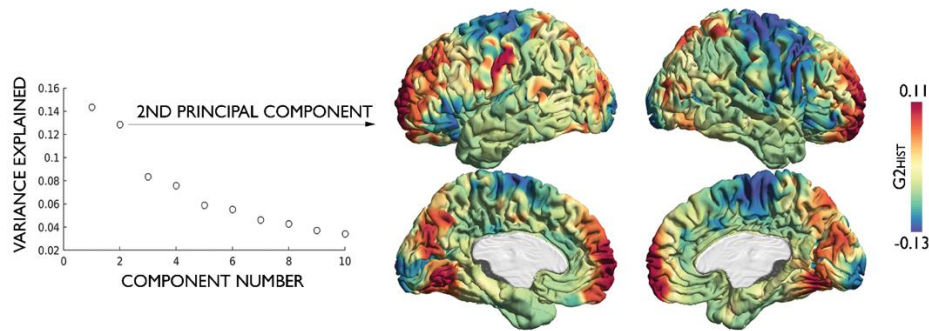


**FIGURE S3.** Robustness of  $G1_{HIST}$  to parameter variation. **(A)**  $MPC_{HIST}$  matrix instability using between 10 and 100 intracortical surfaces.  $G1_{HIST}$  was consistent regardless of the number of intracortical surfaces used, as shown by the strong spatial correlation of the 18-, 54- and 91-surface solutions (all  $r>0.97$ , all  $p<0.001$ ). **(B)** Correlation matrix depicting the high correspondence of  $G1_{HIST}$  solutions with 70-95% row-wise matrix thresholding ( $0.95<r<1$ , all  $p<0.001$ ). **(C)** Estimation of  $G1_{HIST}$  from 20488 vertices resulted in a consistent  $G1_{HIST}$  to the 1012 parcel construction pipeline ( $r=0.87$ ,  $p<0.001$ ). **(D)** The 200μm, 300μm and 400μm resolution BigBrain datasets were characterised as lower resolution replications, and  $G1_{HIST}$  was found to be highly correlated across these resolutions (all  $r>0.81$ , all  $p<0.001$ ).

### A) SECOND PRINCIPAL COMPONENT OF MPC<sub>HIST</sub> (G2<sub>HIST</sub>)



### B) FIRST TWO MPC<sub>HIST</sub> COMPONENTS

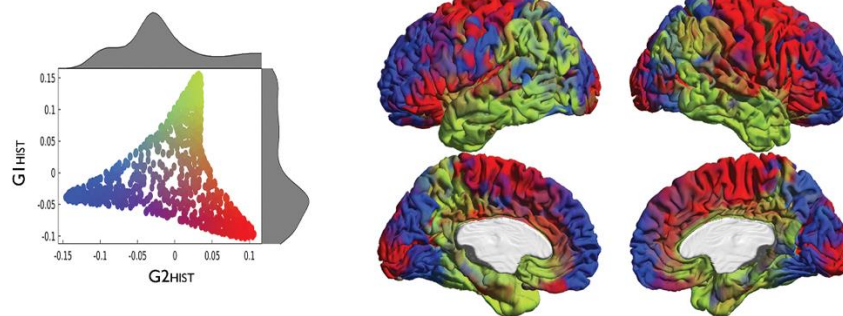


**FIGURE S4.** (A) The second principal component, accounting for 12.7% of variance in MPC<sub>HIST</sub> components, is projected on the BigBrain midsurface. (B) Scatterplot depicting the first two embedding gradients, with corresponding probability density functions. The second gradient divides the lower-order areas of the first gradient, insomuch that somatomotor and primary visual areas (*red*) are separated from ventral prefrontal areas and secondary visual areas (*blue*).

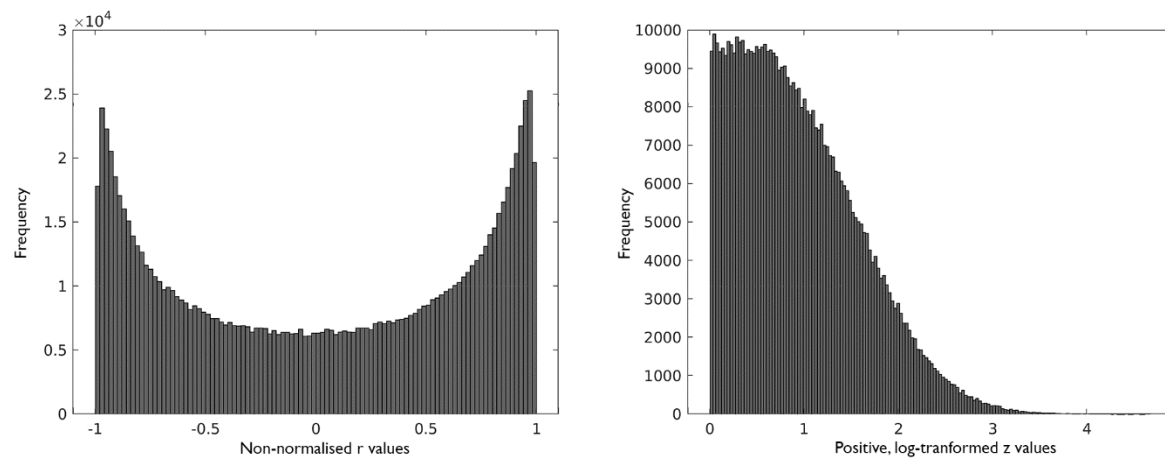
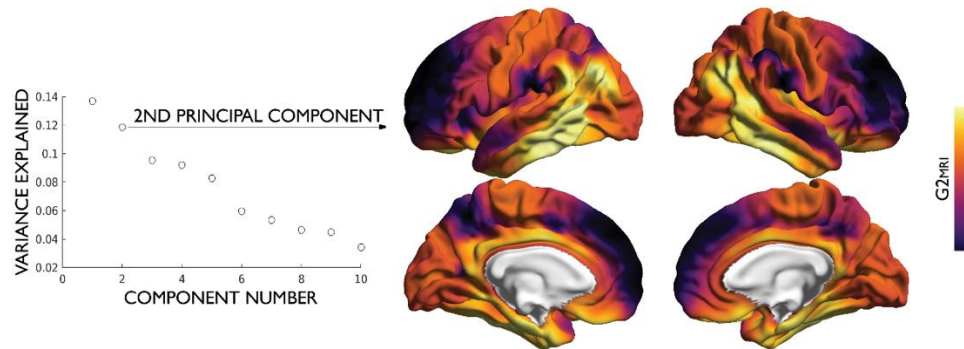


**FIGURE S5.** Distribution of values in  $MPC_{MRI}$  matrix. (*Left*) Frequency of  $r$  values calculated by Pearson product moment correlation coefficient of the nodal intensity profiles, controlling for the average intensity profile. (*Right*) Frequency of positive  $z$  values following log transformation of  $r$  values.



## A) SECOND PRINCIPAL COMPONENT OF MPC<sub>MRI</sub> (G2<sub>MRI</sub>)



## B) FIRST TWO MPC<sub>MRI</sub> COMPONENTS

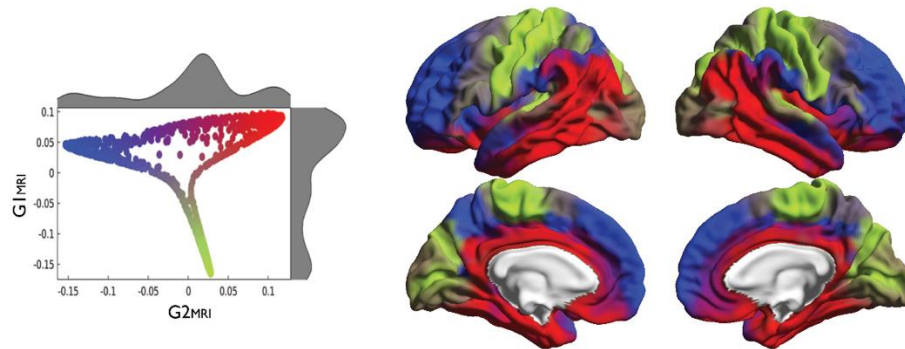


**FIGURE S6. (A)** The second principal component, accounting for 11.7% of variance in MPC<sub>MRI</sub> components, projected on the conte69 midsurface. **(B)** Scatterplot depicting the first two embedding gradients, with corresponding probability density functions. The second gradient divides the higher-order areas of the first gradient, insomuch that the cingulate, orbitofrontal cortex and the inferior temporal gyrus (*red*) are separated from the prefrontal cortex, precuneus, temporo-parietal junction and superior temporal gyrus (*blue*).

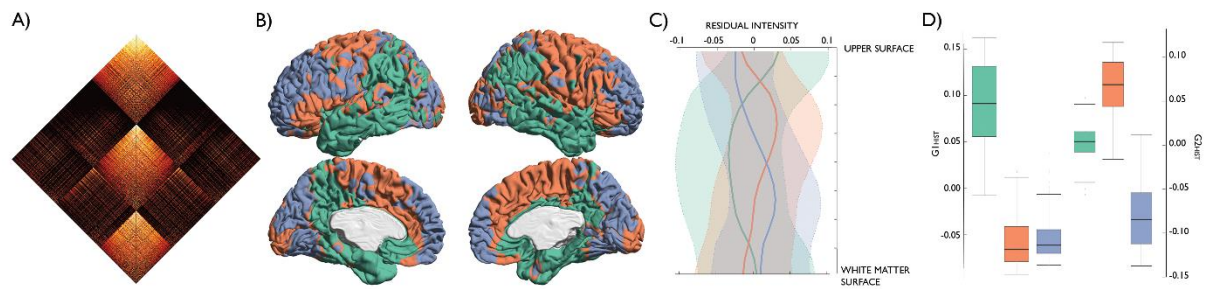


**FIGURE S7.** Community structure of the MPC<sub>HIST</sub>. **(A)** MPC<sub>HIST</sub> matrix sorted by community membership. **(B)** Modular decomposition of MPC<sub>HIST</sub> projected on the BigBrain midsurface. **(C)** Mean $\pm$ sd of residual intensity profile for each module, after correction for the midsurface y-coordinate and demeaning. **(D)** Boxplot depicts the unique positions of modules along the first two principal gradients.

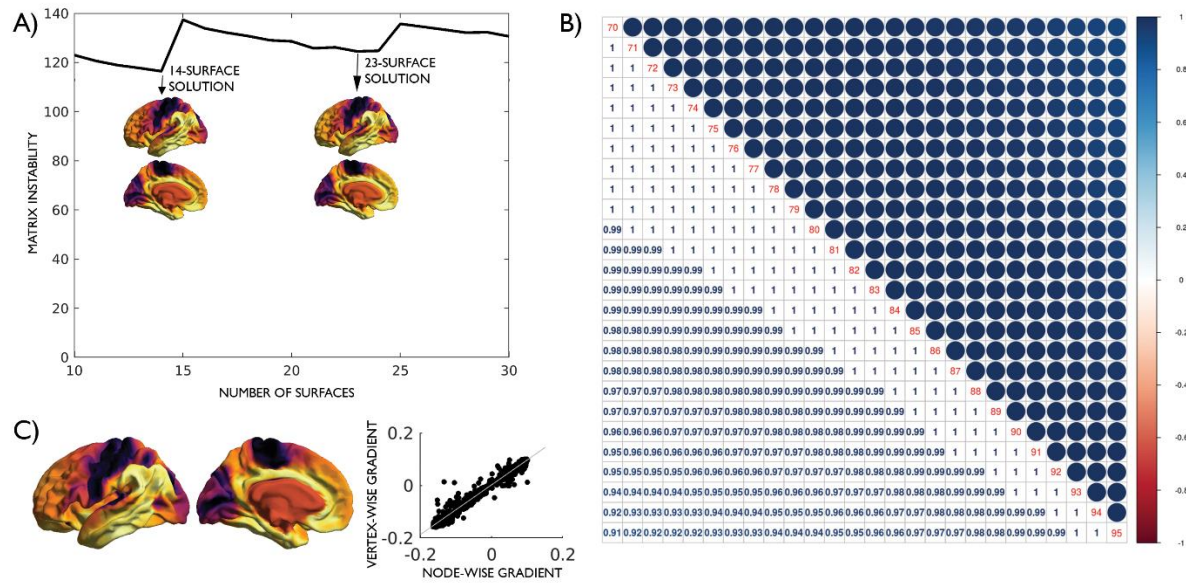


**FIGURE S8.** Robustness of  $G1_{MRI}$  to parameter variation. (A)  $MPC_{MRI}$  matrix instability using between 10 and 30 intracortical surfaces.  $G1_{MRI}$  was consistent regardless of the number of intracortical surfaces used, as shown by the strong spatial correlation of the 14- and 23-surface solutions ( $r=0.98$ ,  $p<0.001$ ). (B) Correlation matrix depicting the high correspondence of  $G1_{MRI}$  solutions with 70-95% row-wise matrix thresholding ( $0.91<r<1$ , all  $p<0.001$ ). (C) Estimation of  $G1_{MRI}$  from 20464 vertices resulted in a consistent  $G1_{MRI}$  to the 1012 parcel construction pipeline ( $r=0.98$ ,  $p<0.001$ ).

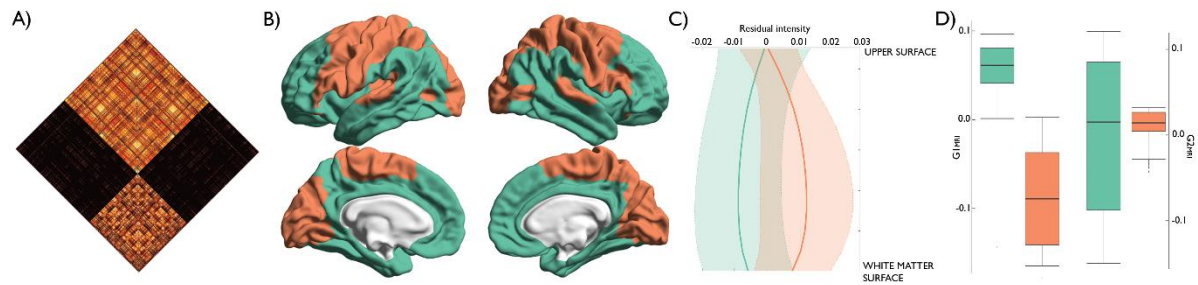


**FIGURE S9.** Community structure of the MPC<sub>MRI</sub>. **(A)** MPC<sub>MRI</sub> matrix sorted by community membership. **(B)** Modular decomposition of MPC<sub>MRI</sub> projected on the conte69 midsurface. **(C)** Mean $\pm$ sd of residual intensity profile for each module, after demeaning. **(D)** Boxplot depicts the unique positions of modules on the first, but not the second, principal component.



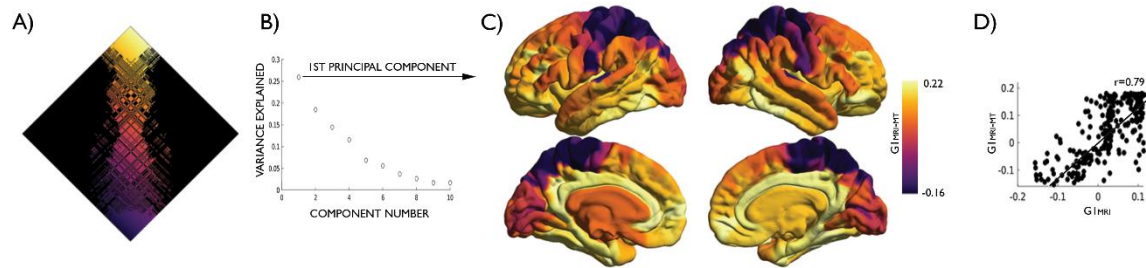


**FIGURE S10.** Independent replication of  $G1_{MRI}$ , using magnetisation transfer (MT) data. **(A)** Gradient ordered normalised angle matrix. **(B)** Variance explained by embedding components. **(C)** First principal gradient ( $G1_{MRI-MT}$ ) projected onto conte69 midsurface. **(D)** Scatterplot depicting the strong correlation between the  $G1_{MRI}$  (reconstructed with the 308 parcellation scheme) and  $G1_{MRI-MT}$  ( $r=0.79$ ,  $p<0.001$ ).

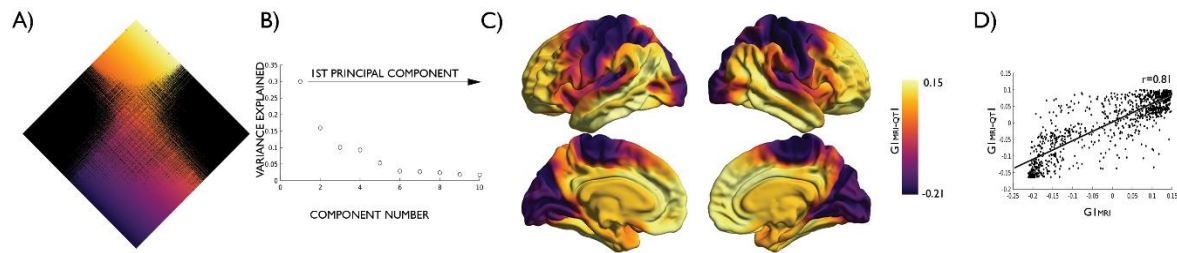


**FIGURE S11.** Independent replication of  $G1_{MRI}$ , using quantitative T1 images. **(A)** Gradient ordered normalised angle matrix. **(B)** Variance explained by embedding components. **(C)** First principal gradient ( $G1_{MRI-QT1}$ ) projected onto conte69 midsurface. **(D)** Scatterplot depicting the strong correlation between the  $G1_{MRI}$  and  $G1_{MRI-QT1}$  ( $r=0.81$ ,  $p<0.001$ ).

**TABLE S1.** Individual predictors in a multiple regression model of G1<sub>HIST</sub> by levels of laminar differentiation

	Estimate	Std. Error	t value	Pr(> t )
Mesulam: idiotypic	0.05651	0.004813	11.74	7.032e-30
Mesulam: unimodal	-0.01105	0.003903	-2.832	0.004723
Mesulam: heteromodal	-0.005509	0.003352	-1.644	0.1006
Mesulam: paralimbic	-0.04945	0.006359	-7.777	1.867e-14

**TABLE S2.** Individual predictors in a multiple regression model of G1<sub>HIST</sub> by classes of cytoarchitecture

	Estimate	Std. Error	t value	Pr(> t )
Von Economo: motor	0.07335	0.008904	8.237	5.589e-16
Von Economo: association <sup>1</sup>	-0.0005984	0.003267	-0.1832	0.8547
Von Economo: association <sup>2</sup>	-0.02703	0.00537	-5.034	5.714e-07
Von Economo: secondary sensory	0.017	0.004712	3.607	0.000325
Von Economo: primary sensory	0.04783	0.008826	5.419	7.53e-08
Von Economo: limbic	-0.06474	0.007497	-8.636	2.32e-17
Von Economo: insular	-0.02524	0.01259	-2.004	0.04531

<sup>1</sup> Frontal and temporal association areas, displayed in yellow (**FIGURE 2**)

<sup>1</sup> Parietal and superior temporal association, displayed in purple (**FIGURE 2**)

**TABLE S3.** Individual predictors in a multiple regression model of  $G1_{MRI}$  by levels of laminar differentiation

	Estimate	Std. Error	t value	Pr(> t )
Mesulam: idiotypic	-0.06807	0.005734	-11.87	1.76e-30
Mesulam: unimodal	-0.03628	0.003094	-11.73	7.847e-30
Mesulam: heteromodal	0.01026	0.003598	2.851	0.004444
Mesulam: paralimbic	0.09981	0.004438	22.49	8.103e-91

**TABLE S4.** Individual predictors in a multiple regression model of  $G1_{MRI}$  by classes of cytoarchitecture

	Estimate	Std. Error	t value	Pr(> t )
Von Economo: motor	0.1486	0.0086	17.28	1.251e-58
Von Economo: association <sup>1</sup>	-0.01441	0.003227	-4.467	8.831e-06
Von Economo: association <sup>2</sup>	0.001541	0.005227	0.2948	0.7682
Von Economo: secondary sensory	-0.008014	0.004666	-1.718	0.08619
Von Economo: primary sensory	0.0974	0.008251	11.8	3.57e-30
Von Economo: limbic	-0.07451	0.007277	-10.24	1.865e-23
Von Economo: insular	-0.05544	0.01284	-4.316	1.746e-05

<sup>1</sup> Frontal and temporal association areas, displayed in yellow (**FIGURE 2**)

<sup>1</sup> Parietal and superior temporal association, displayed in purple (**FIGURE 2**)



**TABLE S5.** Statistical outcome of paired t-tests between  $G1_{MRI}$  and  $G1_{FUNC}$  within each functional community, taken across individuals.

<b>Functional community</b>	<b>t-statistic</b>	<b>2.5% CI</b>	<b>97.5% CI</b>
Visual	-8.3215	-76.998	-47.508
Somatomotor	-10.32	-78.836	-53.551
Dorsal attention	-4.6335	-35.345	-14.249
Salience	-29.099	-202.85	-177.11
Limbic	-22.42	-115.27	-96.641
Frontoparietal	30.123	135.8	154.82
Default mode	54.445	165.76	178.21